Contents lists available at ScienceDirect

Deep-Sea Research I

Testing models of thorium and particle cycling in the ocean using data from station GT11-22 of the U.S. GEOTRACES North Atlantic section

Paul Lerner [a,*], Olivier Marchal [a], Phoebe J. Lam [b], Robert F. Anderson [c], Ken Buesseler [a], Matthew A. Charette [a], R. Lawrence Edwards [d], Christopher T. Hayes [e], Kuo-Fang Huang [f], Yanbin Lu [d], Laura F. Robinson [g], Andrew Solow [a]

[a] Woods Hole Oceanographic Institution, Woods Hole, MA 02543, USA
[b] University of California Santa Cruz, Santa Cruz, CA 95064, USA
[c] Lamont-Doherty Earth Observatory, Columbia University, Palisades, NY 10964, USA
[d] University of Minnesota, Minneapolis, MN 55455, USA
[e] Massachusetts Institute of Technology, Cambridge, MA 02139, USA
[f] Institute of Earth Sciences, Academia Sinica, Nangang, Taipei 11529, Taiwan
[g] University of Bristol, Bristol BS8 1TH, UK

ARTICLE INFO

ABSTRACT

Thorium is a highly particle-reactive element that possesses different measurable radio-isotopes in seawater, with well-constrained production rates and very distinct half-lives. As a result, Th has emerged as a key tracer for the cycling of marine particles and of their chemical constituents, including particulate organic carbon.

Here two different versions of a model of Th and particle cycling in the ocean are tested using an unprecedented data set from station GT11-22 of the U.S. GEOTRACES North Atlantic Section: (i) ^{228,230,234}Th activities of dissolved and particulate fractions, (ii) ^{228}Ra activities, (iii) ^{234,238}U activities estimated from salinity data and an assumed ^{234}U/^{238}U ratio, and (iv) particle concentrations, below a depth of 125 m. The two model versions assume a single class of particles but rely on different assumptions about the rate parameters for sorption reactions and particle processes: a first version (V1) assumes vertically uniform parameters (a popular description), whereas the second (V2) does not. Both versions are tested by fitting to the GT11-22 data using generalized nonlinear least squares and by analyzing residuals normalized to the data errors.

We find that model V2 displays a significantly better fit to the data than model V1. Thus, the mere allowance of vertical variations in the rate parameters can lead to a significantly better fit to the data, without the need to modify the structure or add any new processes to the model. To understand how the better fit is achieved we consider two parameters, $K = k_1/(k_{-1} + \beta_{-1})$ and K/P, where k_1 is the adsorption rate constant, k_{-1} the desorption rate constant, β_{-1} the remineralization rate constant, and P the particle concentration. We find that the rate constant ratio K is large ($\geqslant 0.2$) in the upper 1000 m and decreases to a nearly uniform value of ca. 0.12 below 2000 m, implying that the specific rate at which Th attaches to particles relative to that at which it is released from particles is higher in the upper ocean than in the deep ocean. In contrast, K/P increases with depth below 500 m. The parameters K and K/P display significant positive and negative monotonic relationship with P, respectively, which is collectively consistent with a particle concentration effect.

© 2016 Elsevier Ltd. All rights reserved.

1. Introduction

Roughly 20–25% of carbon fixed photosynthetically by phytoplankton in near surface-waters is estimated to sink as particles to depths below 100 m, with approximately 10% of this sinking material reaching the sediments (Bishop, 2009). The sinking and subsequent remineralization of particulate organic matter strongly influence the vertical concentration gradients of chemical constituents in the ocean, including dissolved inorganic carbon, nutrients, and dissolved oxygen. Therefore, understanding the processes that control the cycling of particles and the exchange of elements between the dissolved and particulate phases is essential in order to understand the distribution of these constituents in the ocean.

The processes that impact marine particles include, e.g., (dis)aggregation, remineralization, dissolution, and gravitational sinking. The

* Correspondence to: Department of Marine Chemistry and Geochemistry, Woods Hole Oceanograic Institution, 266 Woods Hole Road, Clark 448 (MS#25), Woods Hole, MA, USA. Tel.: +1 508 289 3278.
E-mail address: plerner@whoi.edu (P. Lerner).

radioactive isotopes of thorium have for a long time been used to study these processes (for reviews see Savoye et al. (2006); Lam and Marchal (2014)). Thorium is highly particle reactive in seawater, and its isotopes are characterized by widely different half-lives: $t_{1/2} = 24.101 \pm 0.025$ days for ^{234}Th (Knight and Macklin, 1948), $75,584 \pm 110$ yr for ^{230}Th (Cheng et al., 2013), and 1.910 ± 0.002 yr for ^{228}Th (Kirby et al., 2002). Additionally, the sources of these thorium isotopes in the ocean are relatively well understood. ^{234}Th, ^{230}Th, and ^{228}Th are produced in situ by radioactive decay of ^{238}U, ^{234}U, and ^{228}Ra, respectively. Since uranium seems to behave quasi-conservatively in the ocean (Ku et al., 1977; Delanghe et al., 2002), the ^{234}U and ^{238}U activities are often estimated from salinity (Chen et al., 1986; Owens et al., 2011), whereas the ^{228}Ra activity is generally measured directly (Henderson et al., 2013). Another potential source of ^{230}Th is the dissolution of lithogenic materials, although this contribution appears negligible except in surface waters close to mineral dust sources (Hayes et al., 2013). The high particle reactivity of Th combined with multiple isotopes that have a wide range of half-lives makes it particularly well suited to study the variety of processes that affect particles. For example, ^{230}Th has found several applications in paleo-oceanography. These include using ^{230}Th to correct for sediment lateral redistribution (e.g., François et al., 2004) and (in concert with ^{231}Pa) to estimate biological productivity (e.g., Kumar et al., 1993, 1995) and aspects of ocean circulation (e.g., Yu et al., 1996).

The concept of scavenging, i.e., the attachment of trace metals to sinking particles and their subsequent removal to the sea floor, was proposed by Goldberg (1954). Subsequently, there has been widespread recognition of the importance of scavenging in controlling the distribution of trace metals in the ocean (Krauskopf, 1956; Turekian, 1977). Bhat et al. (1969) concluded from ^{234}Th data obtained from the Arabian Sea, Java sea, Australian coast, Wharton Sea, and the Tasmania coast, that the distribution of ^{234}Th is controlled by adsorption of thorium onto particles. They considered an irreversible scavenging model for particulate ^{234}Th, which explained the deficit of ^{234}Th relative to ^{238}U in the surface mixed layer. Their model, however, was based on the assumption that all ^{234}Th is adsorbed onto particles. Krishnaswami et al. (1976), using ^{234}Th data from the Pacific GEOSECS expedition, estimated particulate ^{234}Th to be only 10–20% of the total activity of ^{234}Th (dissolved and particulate). They also found ^{230}Th in the particulate phase to increase approximately linearly with depth in the water column. Based on their observations, they proposed a one-dimensional (vertical) scavenging model for particulate thorium, similar to that of Bhat et al. (1969) but with an added scavenging term to account for the existence of both dissolved and particulate phases.

Nozaki et al. (1981), using data from the western North Pacific, and Bacon and Anderson (1982), using data from the Panama and Guatemala Basins, observed that the activities of ^{230}Th in both dissolved and particulate forms increase generally with depth. This observation necessitated a revision of the scavenging model and prompted the authors to develop a reversible exchange model to account for the observed vertical distributions of dissolved and particulate ^{230}Th. The innovation in this model was a term for the loss of thorium from the particles (one particle class) through desorption and (or) remineralization. Since then, the reversible exchange model has become a popular description of thorium isotope cycling in the oceanic water column, and many studies used this model in combination with a "ventilation" term in the interpretation of ^{230}Th and ^{231}Pa data (e.g., Rutgers van der Loeff and Berger, 1993; Scholten et al., 1995, 2008; Vogler et al., 1998; Moran et al., 2002; Hayes et al., 2015a).

Nevertheless, there has been extensive modifications to the reversible exchange model with one particle class. Clegg and Whitfield (1990) modeled thorium and particles in both small and large size classes. Included in their model are terms for the

aggregation of small particles and disaggregation of large particles. More recently, Burd et al. (2000) presented a "coupled adsorption-aggregation" model, in which a particle size spectrum (particle size ranging from less than 10^{-2} to $53 \ \mu m$) is represented in order to interpret field observations of the particulate organic carbon (POC) to ^{234}Th ratio.

Observational estimates of the rate constants of thorium and particle cycling in the ocean display large variations. They range from 0.1 to 1 yr^{-1} for adsorption and 1–10 yr^{-1} for desorption (Nozaki et al., 1987; Bacon and Anderson, 1982; Murnane et al., 1990, 1994; Murnane, 1994), 1–100 yr^{-1} for remineralization (Clegg et al., 1991), 0.1–100 yr^{-1} for aggregation, and 1–2500 yr^{-1} for disaggregation (Nozaki et al., 1987; Murnane et al., 1990; Cochran et al., 1993; Murnane et al., 1996; Cochran et al., 2000). Likewise, estimates of the sinking speed of bulk particles, including all sizes, vary widely, from 300 to 900 m yr^{-1} (Krishnaswami et al., 1976, 1981; Rutgers van der Loeff and Berger, 1993; Scholten et al., 1995; Venchiarutti et al., 2008). For the average sinking speed of particles greater than 45 μm in diameter, McDonnell and Buesseler (2010) found values from 10 to 150 m d^{-1} in waters near the west Antarctic Peninsula. Turner (2002) reported an even larger range, from less than tens to over thousands m d^{-1}, for the sinking velocity of fecal pellets. These large variations are a current impediment to any attempt to develop large-scale models of particle and biogeochemical processes in the ocean.

In a series of studies, R. Murnane and colleagues pioneered the use of inverse methods in order to estimate rate constants of particle and thorium cycling in the ocean (Murnane et al., 1990, 1994, 1996; Murnane, 1994). Using a generalized nonlinear least squares technique (Algorithm of Total Inversion or ATI) (Tarantola and Valette, 1982), Murnane (1994) performed an inversion of Th and particle data from Station P (50°N, 145°W) in the Gulf of Alaska. He compared solutions obtained from the ATI with two other regression techniques: ordinary least squares and a regression procedures by Wolberg (1967). He found that the solution obtained from the ATI was both more realistic and consistent with prior estimates of the rate constants and with data from station P than solutions obtained from the other techniques.

The adequacy of the ATI to infer rate constants of sorption reactions, however, was questioned by Athias et al. (2000a, 2000b). These authors reported that a least squares approach could not recover rate parameters of a model of Al (another relatively insoluble trace metal) cycling from a simulated data set generated by the same model. They concluded that the generalized least squares approach of Tarantola and Valette (1982) could not be applied to their problem. In contrast, Marchal and Lam (2012) succeeded in inferring rate parameters using the ATI from simulated Th and particle data. Their study suggests that field observations could be used to constrain rate parameters of Th and particle processes in the ocean. Furthermore, they concluded that measurements of particle and ^{228,230,234}Th concentrations in different size fractions, such as generated during GEOTRACES, should significantly improve the precision of the rate parameters inferred relative to *a priori* estimates.

The differences between the results of Athias et al. (2000b) and Marchal and Lam (2012) were discussed by Marchal and Lam (2012). These authors found that relatively large prior errors in the rate parameters in combination with the constraint that the model equations be imposed exactly can prevent the ATI from converging to a stable solution. Thus differences in assumptions about the prior errors between these two studies may have led to different results regarding the adequacy of the ATI to infer rate parameters. Besides Murnane (1994), Murnane et al. (1994, 1996), and Marchal and Lam (2012), other studies have successfully applied the ATI to oceanographic problems (e.g., Mercier, 1986, 1989; Mercier et al., 1993; Paillet and Mercier, 1997; Marchal et al., 2007).

Here we rejuvenate the approach first applied by Murnane (1994) to constrain aspects of thorium and particle cycling from the extensive data set collected at station GT11-22 of the U.S. GEOTRACES North Atlantic Section (GA03) (Boyle et al., 2015). Station GT11-22 was chosen because it is an open ocean station that appears to have relatively little influence from hydrothermal vents near the Mid-Atlantic Ridge and from the Mauritanian Up-welling, both of which may be regions that exhibit enhanced scavenging due to processes not encapsulated by the reversible exchange model (e.g., Hayes et al., 2015a; Lam et al., 2015). The GT11-22 data include ^{234,230,228}Th activities in dissolved ($<0.8\ \mu$m) and particulate (0.8–51 μm) phases, particle concentration in the small ($<51\ \mu$m) and large ($>51\ \mu$m) size fractions, measurements of dissolved ^{228}Ra, and ^{234,238}U activities estimated from salinity data. We feel that there is as of yet insufficient data to constrain a model that deals with Th and particles in both small and large particle fractions. Thus, we use the data (collected at and below 125 m) in order to test two versions of a $1 - D$ (vertical) model of Th and particle cycling that considers one particle class with either vertically uniform (model V1) or nonuniform (model V2) parameters. Specifically, we test whether the fit of model V2 to radiochemical and particle data is significantly better than that of model V1 given the larger number of degrees of freedom of a model with variable parameters. The model is similar to that used by Bacon and Anderson (1982), except that remineralization and desorption are treated separately. The model therefore neglects potentially important effects such as lateral transport. The purpose of this study is to quantify the improvement of the model when the rate parameters are allowed to vary with depth. This way, we provide a test to the commonly held assumption that the rate parameters of Th and particle cycling are uniform along the oceanic water column (e.g., Nozaki et al., 1987; Cochran et al., 1993, 2000; Hayes et al., 2015b).

This paper is organized as follows. In Section 2, the GT11-22 data, the vertical interpolation, the model of particle and Th cycling, and the inverse method used to combine the data and the model are described. In Section 3, each version of the model is fitted to the data, considering errors in the data and in their vertical interpolation. A range of measures of goodness of fit are calculated in order to test the consistency of each model version with the data. In Section 4, we discuss the robustness of the tests, their implications for oceanic Th geochemistry, and the depth-dependent budgets of ^{228,230,234}Th at station GT11-22. An attempt to interpret particle and Th isotope residuals of the fit in terms of processes missing in the model is also undertaken. Conclusions follow in Section 5.

2. Methods

2.1. Hydrographic setting

We use the data collected aboard the R/V Knorr in November 2011 at station GT11-22 (19°26′N, 29°22′W, water depth of 5014 m), approximately 700 km northwest of Cape Verde (Fig. 1). This station is situated in the southeast portion of the North Atlantic subtropical gyre, which is under the influence of the southwestward flow of the Northern Equatorial Current (NEC, Stramma et al. (2005)). The potential temperature (θ) and salinity (S) measured by the CTD at station GT11-22 (Fig. 2) reveal the presence of distinct water masses, defined here according to Jenkins et al. (2015). Between 80 and 554 m, the North Atlantic Central Water (NACW) and Atlantic Equatorial Water (AEW) are carried to station GT11-22 by the NEC (Schmitz and McCartney, 1993; Stramma et al., 2005). In this depth range, NACW represents between 71% and 98% of the total mass according to the water property analysis of Jenkins et al. (2015). The "kink" in the $\theta - S$ diagram at about 230 m ($\theta \simeq 15\ ^\circ$C, $S \simeq 36$) may be due to the replacement of NACW by AEW, decreasing the relative abundance of NACW from about 88% to 71% at that depth. Jenkins et al. (2015) estimated that east of 22°W, nearly all water down to 500 m is AEW. While station GT11-22 is near 30°W, it is well within the influence of AEW, which contributes about 30% of the thermocline waters at this site. Between 609 and 904 m, the Mediterranean Outflow Water (MOW), the Antarctic Intermediate Water (AAIW), and the Irminger Sea Water (ISW) become dominant. The transition between the thermocline (NACW and AEW) and intermediate waters is not conspicuous in the $\theta - S$ diagram, largely because the effect of the relatively salty and warm MOW tends to be offset by the fresher and colder AAIW. Between 940 and 1200 m, the Upper Circumpolar Deepwater (UCDW) and the Upper Labrador Sea Water (ULSW) become important. Salinity increases with depth because the relatively fresh AAIW, the dominant component at shallower depths, decreases to about 0% at 1200 m (Jenkins et al.,
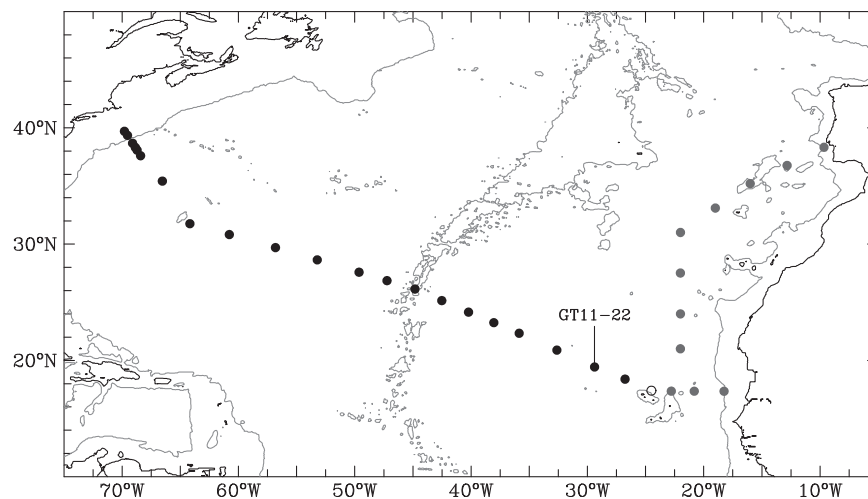

Fig. 1. Stations occupied by the R/V Knorr during the GEOTRACES North Atlantic section. The latitude and longitude of the stations are from http://data.bco-dmo.org/jg/dir/BCO/GEOTRACES/NorthAtlanticTransect/. The grey dots show the stations occupied during the first leg (October 2010) and the black dots show the stations occupied during the second leg (November 2011). The open circle is both station 12 of the first leg and station 24 of the second leg. The data analyzed in this paper originate from station GT11-22, northwest of Cape Verde. The solid lines show the coastline (dark) and the 3000-m isobath (light) (bathymetric data are from http://www.ngdc.noaa.gov/mgg/global).
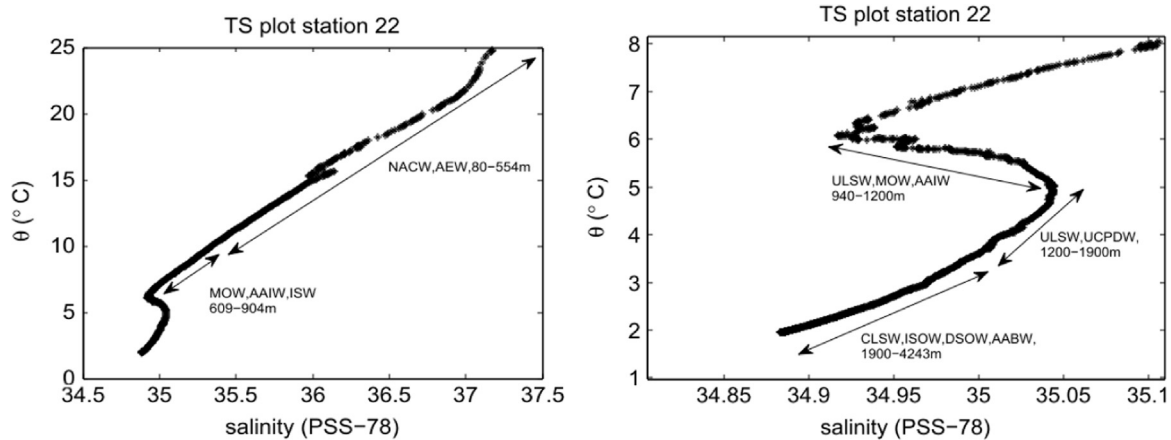
Fig. 2. Plot of potential temperature vs. salinity for station GT11-22. Arrows indicate the estimated range of water masses, with labels and the depth ranges. The left panel shows the $\theta - S$ plot from the surface to a depth of 904 m. The right panel shows the $\theta - S$ plot below 8 °C. Data from Jenkins et al. (2015).

2015). Nearly all water is comprised of ULSW and UCDW between 1200 and 1900 m. The deep water masses below 2000 m include the Classical Labrador Sea Water (CLSW) and two components of North Atlantic Deep Water: the Denmark Straits Overflow Water (DSOW) and the Iceland-Scotland Overflow Water (ISOW). Finally, the lower 2000 m of the water column at station GT11-22 is bathed by Antarctic Bottom Water (AABW). This water flows northward in the western South Atlantic, crosses the equator, and penetrates into the eastern basins of the North Atlantic through the Vema Fracture Zone cutting the Mid-Atlantic Ridge near 11°N (Schmitz and McCartney, 1993).

2.2. Data

The following systems were used to collect the samples. The particulate, dissolved ^{228}Th, and dissolved ^{228}Ra data used in this paper were obtained from samples collected by large volume in-situ filtration. The dissolved ^{230}Th and ^{234}Th measurements were gathered using 30-L Niskin bottles. For the collection of ^{234}Th samples below 1000 m, these bottles were attached individually to the pump wire at the depths of the in-situ pumps. For the collection of dissolved ^{230}Th samples at all depths and ^{234}Th samples above 1000 m, these bottles were mounted on the ODF/SIO rosette on a separate cast. All Niskin and in-situ pump casts were operated over the course of the 26-hour occupation of the station. These data can be found in the GEOTRACES Intermediate Data Product (Mawji et al., 2015).

2.2.1. Particle concentration

In this paper, P denotes particle concentration in units of μ g m^{-3}. Size fractionated particles were collected by large volume in-situ filtration using a modified dual-flow WTS-LV McLane research pump equipped with 142-mm "mini-MULVFS" filter holders (Bishop et al., 2012). One filter holder was loaded with a 51-μm Sefar polyester mesh prefilter followed by paired Whatman QMA quartz fiber filters (1 μm nominal pore size). The other filter holder was also loaded with another 51-μm polyester prefilter, but followed by paired 0.8-μm Pall Supor800 polyethersulfone filters. The particles retained on the quartz filters were used to analyze total particulate carbon and particulate inorganic carbon, while those retained on the polyethersulfone filters were used to analyze biogenic silica and particulate trace metals (Lam et al., 2015; Ohnemus and Lam, 2015). Particle concentrations were determined from the sum of the chemical dry weight of the major particles phases: particulate organic matter, particulate inorganic carbon, biogenic silica, lithogenic material estimated from total particulate

aluminum, and Fe and Mn oxyhyroxides (Lam et al., 2015).

2.2.2. ^{234}Th and ^{238}U

In this paper, the subscript d (p) designates the Th isotope activity in dissolved (particulate) form in units of dpm m^{-3}, e.g., ^{234}Th$_d$ denotes the activity of ^{234}Th in the $<1\mu$m size fraction (QMA) and ^{234}Th$_p$ denotes the activity of ^{234}Th in the >1 μm size fraction (similar designations are adopted for ^{230}Th and ^{228}Th). ^{234}Th$_{tot}$ designates total (dissolved + particulate) ^{234}Th. Particulate ^{234}Th activities on the 1–51 μm (QMA filter) and >51 μm size fractions from in-situ filtration were determined by beta counting (Maiti et al., 2012; Owens et al., 2015). Small volume (4 L) samples for ^{234}Th$_{tot}$ were obtained using an ODF/SIO Rosette above 1000 m or Niskin bottles hung above the McLane pump below 1000 m, and were also analyzed using beta counting (Owens et al., 2015). ^{238}U is estimated from salinity using the empirical equation derived by Owens et al. (2011),

$$^{238}U = 0.0786(\pm .00446)S - 0.315(\pm 0.158), \tag{1}$$

where ^{238}U is in dpm m^{-3} and S is on the Practical Salinity Scale of 1978. The uncertainties of ^{238}U are estimated by the root mean square error of the linear regression of ^{238}U with salinity (Owens et al., 2011).

2.2.3. ^{230}Th and ^{234}U

Subsamples of polyethersulfone filters were acid digested and co-precipitated with Fe after complete dissolution. Particulate ^{230}Th in the small (0.8–51 μm) size fraction was determined on the subsamples by inductively coupled plasma mass spectrometry (ICP-MS) (Hayes et al., 2015a). Subsamples for dissolved ^{230}Th were obtained using Niskin bottles attached to an ODF/SIO Rosette, and gravity filtered through Pall Acropak 500 filters containing a 0.8-μm prefilter followed by a 0.45-μm filter. Dissolved ^{230}Th was also measured by ICP-MS (Anderson et al., 2012; Shen et al., 2012; Hayes et al., 2015b). Finally, ^{234}U is estimated from ^{238}U by assuming a ^{234}U/^{238}U ratio of 1.147 (Andersen et al., 2010). The uncertainties in ^{234}U are obtained by multiplying the uncertainties in ^{238}U by 1.147, i.e., the effect of the uncertainty in ^{234}U/^{238}U is neglected.

2.2.4. ^{228}Th and ^{228}Ra

Particulate ^{228}Th in the small (1–51 μm) size fraction sampled by in-situ filtration was measured by alpha delayed coincidence counting of QMA filters (Maiti et al., 2015). Dissolved ^{228}Ra and ^{228}Th were collected simultaneously with particles by sorption on MnO$_2$ impregnated acrylic cartridges located downstream of the two filter holders. They were analyzed by alpha delayed

coincidence (^{228}Th) and gamma counting (^{228}Ra) (Henderson et al., 2013; Charette et al., 2015).

2.3. Bulk particulate ^{228,230,234}Th

Observational estimates of ^{228,230,234}Th activities for the whole particulate fraction (sizes >1 μm) are obtained as follows. ^{228,230,234}Th activities have been measured on the small particles (1–51 μm). ^{234}Th data for large particles are available only in the top 900 m, and ^{228,230}Th data for large particles are currently not available. In order to obtain bulk particle data for each Th isotope, the ratio of large (^{234}Th$_{p,l}$) to small particulate ^{234}Th (^{234}Th$_{p, s}$) is calculated from the ^{234}Th$_{p,l}$ and ^{234}Th$_{p,s}$ data available for the upper 900 m and below the euphotic zone (below 125 m, $n=5$). This ratio (mean of 0.19 with a standard deviation of 0.01) is then applied to derive ^{234}Th$_{p,l}$ below 900 m and ^{228,230}Th$_{p,l}$ at all depths, from the measured activities on the small size fraction. The measured or calculated ^{228,230,234}Th$_{p,l}$ is added to the measured ^{228,230,234}Th$_{p,s}$ to obtain total particulate Th for each isotope (e.g., ^{228}Th$_p$ = ^{228}Th$_{p,s}$ + ^{228}Th$_{p,l}$). Additionally, dissolved ^{234}Th (not measured at station GT11-22) is obtained by subtracting ^{234}Th$_p$ from total ^{234}Th and its error is derived by error propagation neglecting error covariance (Bevington and Robinson, 1992).

2.4. Vertical interpolation

The depths at which P, ^{228,230,234}Th$_{d,p}$, ^{234,238}U, and ^{228}Ra data are available do not generally coincide exactly (Appendix A). In order to facilitate the data analysis, the measured (or calculated) values of P, ^{228,230,234}Th$_{d,p}$, ^{234,238}U, and ^{228}Ra are interpolated onto an irregular grid in which each grid point is at a depth where at least one measurement is available. The shallowest and deepest points of the grid are at 125 and 4243 m, respectively. Such a grid is chosen in order (i) to exclude surface waters where processes of particle production, which are outside the scope of this study, occur, and (ii) to avoid the need for data extrapolation. We use an objective interpolation technique (e.g., Wunsch, 2006): an estimate of property x at depth level i, $\hat{x}_i$, is taken as a linear combination of the measurements of that property at all depths, x_k ($k = 1, 2, …, n$),

$$\hat{x}_i = \sum_{k=1}^{n} w_{ik} x_k, \tag{2}$$

where the weighting factors w_{ik} are determined such that the errors have minimum variance.

The interpolation requires the prescription of two matrices: a covariance matrix for the measurement errors and a matrix describing the vertical covariance of the property being interpolated. The first matrix is taken as diagonal, where the diagonal elements are the squared errors in the measurements. The (i,j) element of the second matrix is taken as $\sigma_M^2 e^{-|z_i - z_j|/l_z}$, where σ_M^2 is the variance of the property and l_z is a length scale characterizing its vertical covariance. The quantities σ_M^2 and l_z have the following interpretation. When the interpolation depth is far from the measurement depth, the error in the interpolated value approaches the square root of the field property variance σ_M^2. So, σ_M^2 is the maximum tolerable variance in the gridded (interpolated) data. On the other hand, l_z is an e-folding length scale: if the distance between two depths in the water column increases by l_z, the property covariance between both depths is reduced by a factor of $1/e$.

Fig. 3 shows three interpolation scenarios obtained with $\sigma_M^2 = 0.25\sigma_d^2$, $0.5\sigma_d^2$, or σ_d^2 ($l_z = 1000$ m in all cases), where σ_d^2 is the variance in a particular data set (e.g., the variance in the ^{230}Th$_d$ data). Besides differences in uncertainty in the interpolated values (Fig. 3a–c), the agreement between the interpolated and measured

values at the measurement depths deteriorates as σ_M^2 decreases (Fig. 3d–f). This is because σ_M^2 influences the weight of each measurement in the interpolated values: the larger the variance, the better the ability of the interpolated values to approach the measured values. Thus, increasing σ_M^2 improves the agreement of the interpolated values with the measured values, although each scenario tends to overfit the data according to the normal distribution (Fig. 3d–f). Decreasing σ_M^2 to less than $0.25\sigma_d^2$ (not shown) results in interpolated data errors that are smaller than the uncertainties in the measurements, which is not desirable. Therefore, we retain $\sigma_M^2 \geq 0.25\sigma_d^2$ in this study.

Fig. 4 shows three other interpolation scenarios with the same values of $\sigma_M^2 = 0.5\sigma_d^2$ but with different values of $l_z = 500$ m, 1000 m, or 2000 m. These different length scales capture scenarios in which there is varying vertical correlation between property values at different depths. As l_z increases, the error of the interpolated values decreases (Fig. 4a–c). For the three values of l_z, the interpolated values are consistent with the measured values, although each scenario displays an overfit to the measurements according to the normal distribution (Fig. 4d–f). In this paper, we choose $\sigma_d^2 = 0.5\sigma_M^2$ and $l_z = 1000$ m as our reference interpolation. Different sets of interpolated values of P, ^{228,230,234}Th$_{d,p}$, ^{234,238}U, and ^{228}Ra are considered in Section 3.

Fig. 5 shows the measured and interpolated values of the various radiochemical activities at station GT11-22 ($\sigma_d^2 = 0.5\sigma_M^2$, $l_z = 1000$ m). The measured and interpolated values of ^{230}Th$_d$ and ^{230}Th$_p$ show increases with depth. However, ^{230}Th$_p$ is in general relatively uniform below 2000 m, as is dissolved ^{230}Th below 3500 m. Particulate ^{234}Th decreases generally with depth to 2000 m, and shows reduced variations below. Total ^{234}Th varies between 2100 and 2700 dpm m^{-3}, with no clear systematic changes with depth. Finally, the profiles of dissolved and particulate ^{228}Th generally resemble that of the parent isotope, ^{228}Ra, with maxima in surface and bottom waters and minima at mid-depth.

2.5. Model of thorium and particle cycling

We consider a model of thorium and particle cycling that includes a balance equation for each thorium isotope in each phase (dissolved and particulate), and a balance equation for bulk (large+small) particles (Fig. 6). The model accounts for adsorption of thorium to particles, desorption of Th from particles, radioactive production and decay, remineralization of particles, and sinking of particles. The balance equations are (Nozaki et al., 1981; Bacon and Anderson, 1982)

$$0 = \lambda A_\pi + (k_{-1} + \beta_{-1})A_p - (k_1 + \lambda)A_d, \tag{3a}$$

$$w\frac{\partial A_p}{\partial z} = k_1 A_d - (\beta_{-1} + k_{-1} + \lambda)A_p, \tag{3b}$$

$$w\frac{\partial P}{\partial z} = -\beta_{-1}P. \tag{3c}$$

Here A_d (A_p) is the thorium isotope activity in dissolved (particulate) form (dpm m^{-3}), A_π is the activity of the radioactive parent (dpm m^{-3}), P is the particle concentration (μg m^{-3}), and λ is the radioactive decay constant (yr^{-1}). The rate parameters of the model are the adsorption rate constant (k_1, yr^{-1}), the desorption rate constant (k_{-1}, yr^{-1}), the remineralization rate constant (β_{-1}, yr^{-1}), and the particle sinking speed (w, m yr^{-1}). The presence of the vertical derivative in Eqs. (3b)–(3c) requires the prescription of boundary conditions, which we take as the values of A_p and P at $z = 125$ m. Two model versions are considered: version V1 assumes uniform rate parameters, whereas version V2 allows these parameters to vary with
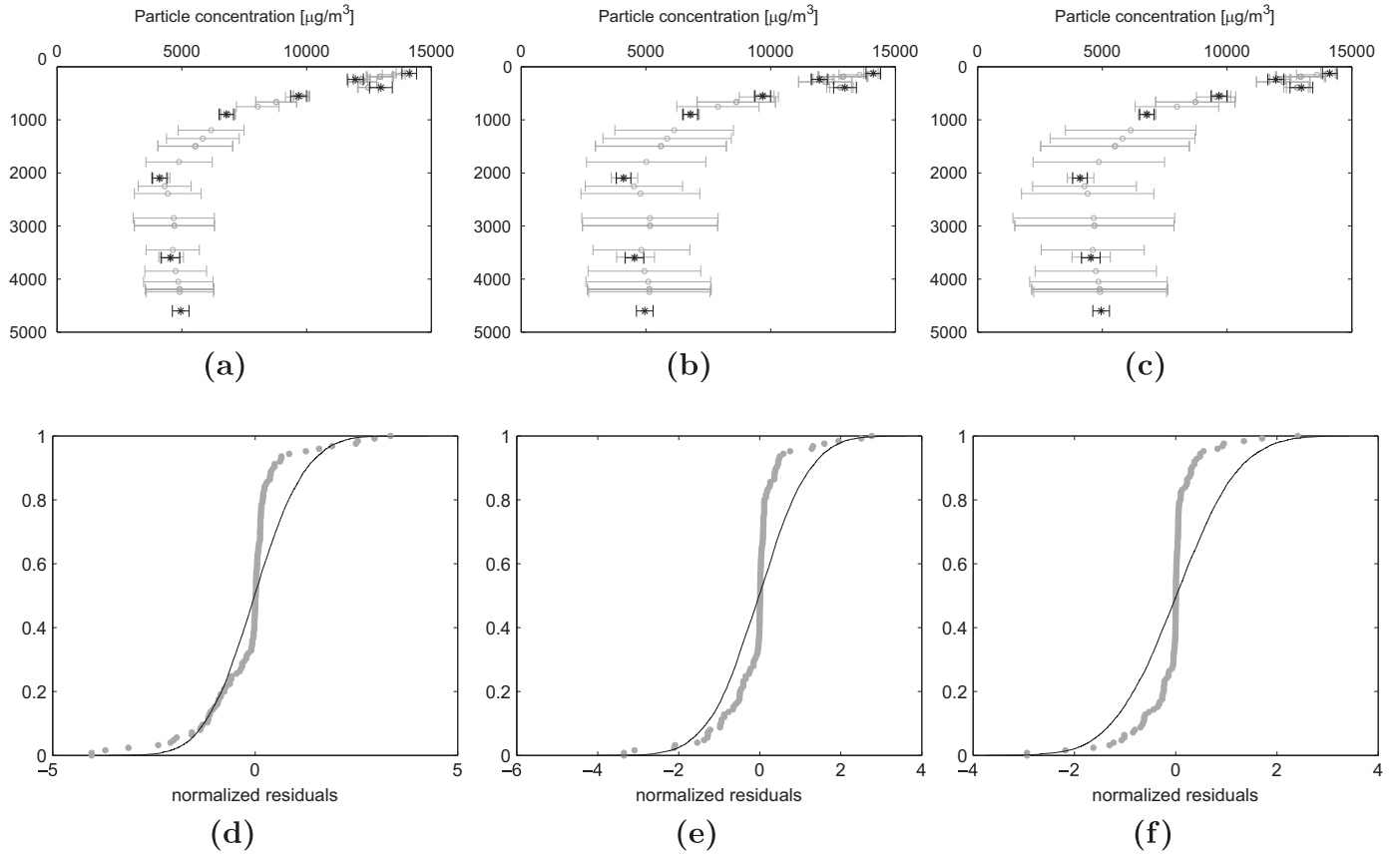
Fig. 3. Top row (a–c): Measured (black asterisks) and interpolated (open circles) values of particle concentration (P) at station GT11-22 for three different field property variances: $\sigma_M^2 = 0.25\sigma_d^2$ (a), $\sigma_M^2 = 0.5\sigma_d^2$ (b), and $\sigma_M^2 = \sigma_d^2$ (c), where σ_d^2 is the variance of P measurements at station GT11-22. A length scale of $l_z = 1000$ m is used for each panel. Horizontal bars show ± 1 standard deviation. Measured particle concentrations are from Lam et al. (2015). The deepest measured value used in the interpolation of particle concentration is at 4600 m. Bottom row (d–f): Distribution function (DF) of the interpolation residuals normalized to measurement errors for all GT11-22 data used in this study. A normalized residual is defined as $(\hat{x}_i - x_{d,i})/\sigma_{d,i}$, where $\hat{x}_i$ is the interpolated value at measurement depth level i, $x_{d,i}$ is the measured value at this level, and $\sigma_{d,i}$ is the error in the measurement at this level. For the three values of σ_M^2, the difference $|\hat{x}_i - x_{d,i}|$ is less than $2\sigma_{d,i}$ for more than 95% of the data, which suggests an overfit (the solid line shows the normal DF).

depth.

Note the various assumptions in the Th and particle cycling model (besides the assumption of uniform rate parameters in model V1). Eqs. (3a)–(3c) rely on steady state and omit the effects of water transport by advection and diffusion. They assume that sorption and remineralization processes obey first-order kinetics. The potential sources of dissolved and particulate Th from lithogenic contributions are taken as negligible. This assumption should be valid for ^{228,234}Th, at least in the surface ocean where the activities of both isotopes are generally large. Following the procedures documented in Roy-Barman et al. (2002) and Hayes et al. (2013), we calculate the percent contribution of lithogenic ^{230}Th to the measured ^{230}Th$_{d,p}$ using dissolved and particulate ^{232}Th data at station GT11-22 (Anderson et al., 2012; Hayes et al., 2015a). We find that lithogenic ^{230}Th$_d$ always accounts for less than 10% of total ^{230}Th$_d$. Lithogenic ^{230}Th$_p$ accounts for up to 30% of total ^{230}Th$_p$ in the upper 500 m, but less than 10% below 500 m. Unless stipulated otherwise, we do not correct ^{230}Th for a lithogenic contribution (the sensitivity of our results to such a correction is examined in Section 4.1.2).

2.6. Inverse method

The ATI (Tarantola and Valette, 1982) is used to combine the Th and particle cycling model (Section 2.5) with the radiochemical and particle measurements at station GT11-22 (Sections 2.2–2.4): model V1 and V2 are fitted to the data, and their respective ability to explain the data is assessed from the residuals of the fit. The rate parameters $(k_1, k_{-1}, \beta_{-1}, w)$ as well as the radiochemical activities and particle concentrations are adjusted so as to obtain the best fit. Thus the particle and radiochemical data are not fixed to their measured (interpolated) values but are allowed to change in the inversion within a range consistent with their estimated uncertainties. This approach allows us to give due consideration to the errors in the radiochemical and particle data when testing model V1 and V2 (see discussion in Lam and Marchal (2014)).

A brief description of the ATI follows. Let $\boldsymbol{x}$ be a vector describing the state of the Th and particle cycles according to the model. The elements of $\boldsymbol{x}$ are the Th isotope activities in the dissolved and particulate phases, the particle concentrations, the parent activities (^{234}U, ^{238}U, ^{228}Ra), as well as the rate parameters $(k_1, k_{-1}, \beta_{-1}, w)$. In model V1, $\boldsymbol{x}$ includes these variables at all depths of the grid at station GT11-22 (Section 2.4), except for the uniform rate parameters. In model V2, $\boldsymbol{x}$ includes these variables at all depths of the grid. The objective is to find a vector $\boldsymbol{x}$ that fits station GT11-22 (interpolated) data given their error statistics, while satisfying the model Eqs. (3a)–(3c) perfectly. This vector is found at a stationary point of the objective function:

$$J = (\boldsymbol{x} - \boldsymbol{x}_0)^T \boldsymbol{C}_0^{-1}(\boldsymbol{x} - \boldsymbol{x}_0) + \boldsymbol{x}^T \boldsymbol{S}^{-1}\boldsymbol{x} - 2\boldsymbol{u}^T \boldsymbol{f}(\boldsymbol{x}). \quad (4)$$

Here, $\boldsymbol{x}_0$ is a vector including prior estimates of the elements in $\boldsymbol{x}$ (in our study, the interpolated data and prior estimates of rate parameters), $\boldsymbol{C}_0$ is the error covariance matrix for the prior estimates (the diagonal elements of $\boldsymbol{C}_0$ are the squared errors in the
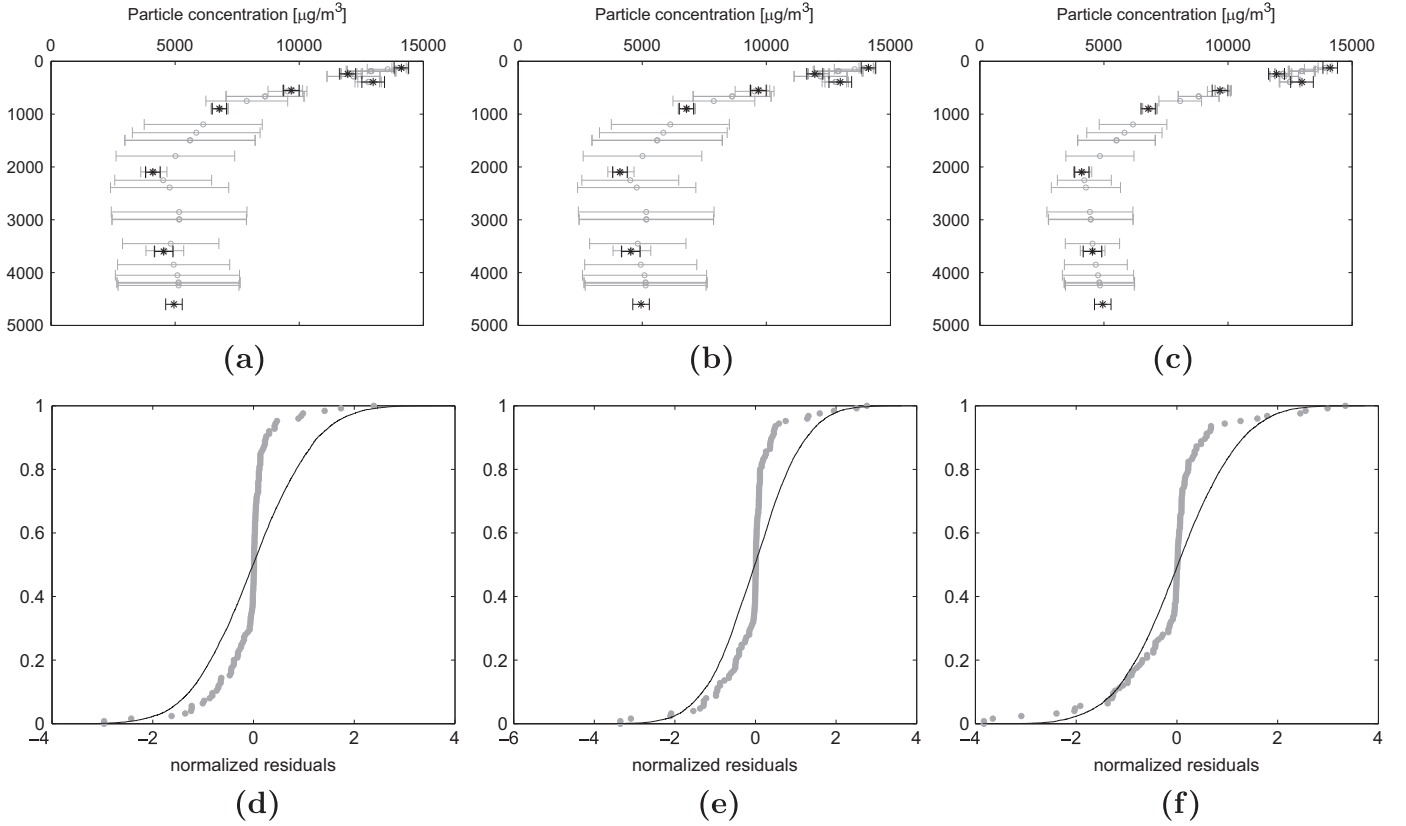
Fig. 4. Same as Fig. 3, but for three different vertical correlation scales: $l_z = 500$ m (a), $l_z = 1000$ m (b), and $l_z = 2000$ m (c). A field property variance of $\sigma_M^2 = 0.5\sigma_d^2$ is used for each panel. Measured particle concentrations are from Lam et al. (2015).

estimates and the off-diagonal elements of C_0 are the covariances between the errors), S^{-1} is another square matrix, u is a vector of Lagrange multipliers, and $f(x) = 0$ is a vector including the difference equations derived from (3a)–(3c), with $w \partial A_p / \partial z$ and $w \partial P / \partial z$ discretized with a first-order backward scheme.

The three terms of the objective function (4) have the following interpretations. The first term represents the deviation of the state vector from its prior estimate, where C_0 plays the role of a weighting factor: the elements of x_0 with small (large) uncertainties contribute strongly (modestly) to the objective function. The second term prescribes a certain amount of smoothing on the vertical variation of some elements of x (see below). Finally, the third term is the hard constraint imposed in the search for a stationary point of J. Thus, we search for a minimum of the sum of the first two terms, subject to the hard constraint $f(x) = 0$. The prior estimates of the rate parameters and their errors are based on observational estimates published in the literature (Table 1; Section 1).

The motive for including the smoothing term $x^T S^{-1} x$ in J is twofold. First, since some of the prior estimates contain large errors, it is possible that some elements of the solution are negative, which is nonsensical in our study. Preliminary inversions have shown that negative values tend to not occur when some smoothing is imposed to the solution. Second, the imposition of smoothing tends to prevent large variations of solution elements on small vertical scales, which do not appear geochemically plausible. Here S^{-1} only acts on the rate parameters ($k_1, k_{-1}, \beta_{-1}, w$). The non-vanishing elements of $x^T S^{-1} x$ have the generic form

$$\gamma \left(x(z_2) - x(z_1) \right)^2, \tag{5}$$

where x represents k_1, k_{-1}, β_{-1}, or w, z_1 and z_2 are two different depths, and the parameter γ trades smoothness of the solution against its proximity to the data. In our study, γ is set equal to 1, unless stipulated otherwise. The effect of γ on our results is

examined in Section 4.1.

The dimensions of the vector x and $f(x)$ are as follows. The number of grid points is 41, but since the shallowest grid point is where the boundary conditions of the model are imposed, the ^{234,238}U, ^{228}Ra, and ^{228,230,234}Th$_d$ activities are defined at 40 depths, while the ^{228,230,234}Th$_p$ activities and P concentrations are defined at all depths. Furthermore, there are 40 equations for each Th isotope in each phase (dissolved and particulate), as well as 40 equations for the particle concentration. As a result, there are $M = 280$ equations (elements of $f(x)$) and $N = 408$ unknowns (elements of x) for model V1, and there are $M = 280$ equations and $N = 564$ unknowns for model V2. In both cases, the fit of the model equations to the data is an underdetermined problem.

The ATI can be derived as follows. The model equations $f(x)$ are linearized, i.e., $f(x_{k+1}) = f(x_k) + F_k(x_{k+1} - x_k)$, where x_{k+1} and x_k denote two different values of x, and F_k is a matrix whose elements are the partial derivatives of the model equations with respect to the elements of x, i.e., the element in the ith row and jth column of F_k is $\partial f_i / \partial x_j$. Setting $\partial J / \partial x = 0$ and $\partial J / \partial u = 0$ then leads to a system of linear algebraic equations from which an iterative procedure to find x can be derived. The solution for x at the $(k+1)$th iteration and its error covariance matrix are given by, respectively:

$$\hat{x}_{k+1} = P_k x_0 + C_{os} F_k^T (F_k C_{os} F_k^T)^{-1} b_k, \tag{6}$$

$$C_{k+1} = P_k C_0 P_k^T, \tag{7}$$

where

$$P_k = C_{os} C_0^{-1} - C_{os} F_k^T (F_k C_{os} F_k^T)^{-1} F_k C_{os} C_0^{-1}, \tag{8}$$
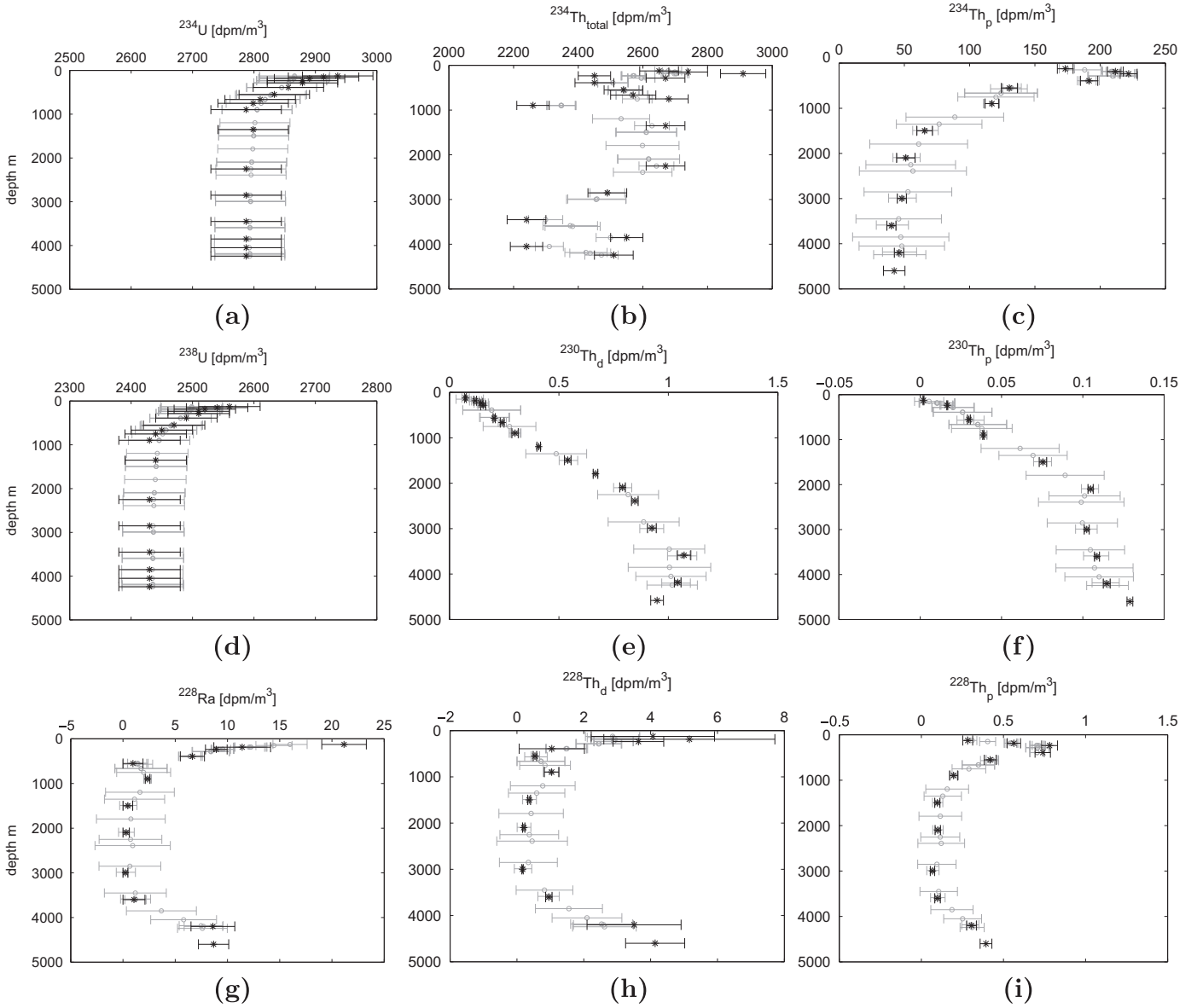
Fig. 5. Profiles of Th isotope activities and their parent activities at station GT11-22. The black asterisks are the measured values. The open circles are the interpolated values obtained with $\sigma_M^2 = 0.5\sigma^2$, $l_z = 1000$ m. Horizontal bars show $\pm$ 1 standard deviation.

$$\boldsymbol{b}_k = \boldsymbol{F}_k \hat{\boldsymbol{x}}_k - \boldsymbol{f}\left(\boldsymbol{x}_k\right), \tag{9}$$

$$\boldsymbol{C}_{os} = (\boldsymbol{C}_0^{-1} + \boldsymbol{S}^{-1})^{-1}. \tag{10}$$

The iterative procedure is initiated at $\hat{\boldsymbol{x}}_{k=0} = \boldsymbol{x}_0$ and terminated when the relative difference between two subsequent values of each element of $\hat{\boldsymbol{x}}$ is less than 1% in absolute magnitude. The estimate of $\boldsymbol{x}$ obtained at this stage is referred to as the solution of the fit of model V1 or V2 to GT11-22 data.

To ensure that the Th and particle equations in $\boldsymbol{f}(\boldsymbol{x}) = \boldsymbol{0}$ have a commensurate effect in the inversion, independent of the choice of units, the elements of $\boldsymbol{x}$ are normalized by their prior values in $\boldsymbol{x_0}$ prior to the operation of the ATI. Accordingly, all elements of $\boldsymbol{x_0}$ are set equal to 1 and all elements of $\boldsymbol{C_0}$ are scaled by the squared errors in the prior estimates. Additionally, each model equation is normalized by the root of the sum of the squared terms in that equation. This normalization scheme forces the leading terms in each equation to be roughly on the same order of magnitude, so that the effect of each equation should be similar in the inversion.

3. Results

In this section, the two versions of the Th and particle cycling model (V1 and V2; Section 2.4) are fitted to the station GT11-22 data (Sections 2.2–2.4) using the ATI (Section 2.5). The fitted values of ^{234,238}U, ^{228}Ra, ^{228,230,234}Th$_{d,p}$ and particle concentration are plotted in Fig. 7 for model V1 and Fig. 8 for model V2. For both versions, convergence to a stable solution is reached after 14 iterations. In order to check whether the model equations are satisfied by the solution given the inevitable numerical errors involved in the matrix operations (6)–(10), the residual of each equation, $f_i(\hat{\boldsymbol{x}}) = \epsilon_i$, is calculated and compared with the maximum term in the corresponding equation. For each fit (V1 or V2), we find that the residual ϵ_i amounts to less that 10^{-3} (in absolute magnitude) of the maximum term for each equation, indicating that the model equations are satisfied to at least the 3rd order.

3.1. Goodness of fit

Two measures of goodness of fit of model V1 and V2 to GT11-22 data are considered. A first measure is the fraction (ϕ below) of
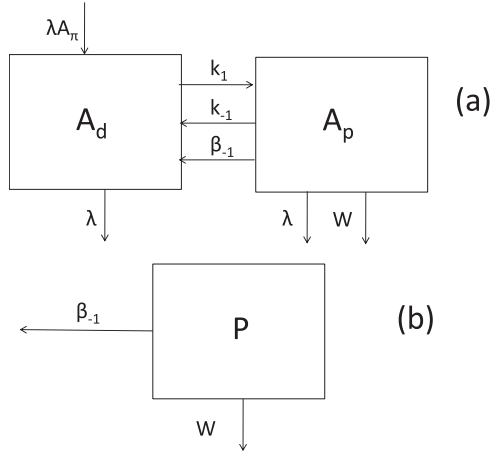
Fig. 6. Schematic diagram of the single-particle class model of Th cycling (a) and particle cycling (b). 'A' and 'P' represent, respectively, the Th isotope activity and the particle concentration in the dissolved fraction ('d') or the particulate fraction ('p'). A_π is the activity of the parent isotope. The other symbols represent the rate parameters of solid-solution exchange (k_1 for adsorption, k_{-1} for desorption) and particle processes (β_{-1} for remineralization, and w for particle sinking). λ is the radioactive decay constant.

Table 1
Prior estimates of rate parameters of Th and particle cycling assumed in this study.

Parameter	Prior estimate	Prior estimate error
k_1 (y^{-1})	0.5	5
k_{-1} (y^{-1})	2	5
β_{-1} (y^{-1})	1	10
w (m y^{-1})	700	400

the normalized residuals that are less than 2 in absolute magnitude, where a normalized residual is defined as

$$r_i = \frac{\hat{x}_i - x_{d,i}}{\sigma_{d,i}}, \ i=1, 2, \ldots, n. \tag{11}$$

Here $\hat{x}_i$ is the estimated value of the ith variable (^{228,230,234}Th$_{d, p}$, ^{234,238}U, ^{228}Ra, and P) in the vector $\hat{\boldsymbol{x}}$ that is obtained from the fit of model V1 or V2 to GT11-22 data, $x_{d,i}$ is the measured (not interpolated) value of this variable, $\sigma_{d,i}$ is the error in this measured value, and n is the number of measured values. The interpretation of ϕ is straightforward. For example, a value of 0.95 for ϕ would mean that the model version being considered can be brought into consistency with 95% of the GT11-22 data given their errors.

The second measure of goodness of fit is the arithmetic average of the difference between the estimated and measured values, normalized by the measurement error:

$$B = \frac{1}{n} \sum_{i=1}^{n} \frac{\hat{x}_i - x_{d,i}}{\sigma_{d,i}}. \tag{12}$$

In general, a relatively large absolute value of B would indicate a relatively large bias of the corresponding model version in describing the GT11-22 data. The quantities ϕ and B are complementary measures of goodness of fit: ϕ describes the overall ability of model V1 or V2 to fit GT11-22 data with no regard for possible under- or over-estimation, whereas B should be indicative of systematic errors in the model versions.

We find that the version of the Th and particle cycling model that assumes vertically uniform rate parameters (model V1) can fit 52–55% of the GT11-22 data ($0.52 \leq \phi \leq 0.55$), where the range reflects varying assumptions for vertical interpolation (Table 2). In contrast, the model version that permits vertical variations in k_1, k_{-1}, β_{-1}, w

(model V2) can explain 73–78% of the GT11-22 data, where the range reflects again varying assumptions about $\sigma_M{}^2$ and l_z.

The model version that allows vertical variations in the rate parameters produces a better fit to the observations than the version that does not. This result holds as the interpolation parameters are varied within plausible ranges, e.g., $0.25\sigma_d^2 \leq \sigma_M^2 \leq \sigma_d^2$ and $500 \text{ m} \leq l_z \leq 2000 \text{ m}$. Moreover, the bias of model V2 ($-0.53 \leq B \leq -0.40$) is always less than for model V1 ($-2.00 \leq B \leq -1.86$), indicating that allowance of vertical variations of k_1, k_{-1}, β_{-1}, and w reduces the systematic errors of the Th and particle cycling model (Table 2).

3.2. Bootstrap test

To compare models V1 and V2, we perform a parametric bootstrap test (Efron and Tibshirani, 1993) of the null hypothesis H_o that V1 is correct against the alternative hypothesis H_1 that V2 is correct. Let $x_{d,i}$ be a measured value with standard deviation $\sigma_{d,i}$ and let $\hat{x}_{1,i}$ be the corresponding fitted value for V1. The goodness of fit of V1 to all n measurements can be determined by:

$$J_d(V1) = \sum_{i=1}^{n} \left(\frac{\ln(x_{d,i}) - \ln(\hat{x}_{1,i})}{\sigma_{\ln(x_{d,i})}} \right)^2, \tag{13}$$

where

$$\sigma_{\ln(x_{d,i})} = \sqrt{\ln\left(1 + \frac{\sigma_{d,i}^2}{x_{d,i}^2}\right)}. \tag{14}$$

is an estimate of the standard deviation of $\ln(x_{d,i})$ (Vanmarcke, 1983). The test statistic used in the parametric bootstrap procedure is:

$$T = J_d(V1) - J_d(V2), \tag{15}$$

where $J_d(V2)$ is the analogue of (13) for V2. The quantity T measures the improvement in fit by relaxing the constraint of parameter uniformity in model V1.

The parametric bootstrap test proceeds by (i) simulating a set of measurements from the fitted model V1,

$$x_{d,i}^* = e^{\ln(\hat{x}_{1,i})+\epsilon_i}, \quad i = 1, 2, \ldots n \tag{16}$$

where ϵ_i is normally distributed with mean 0 and standard deviation $\sigma_{\ln(x_{d,i})}$, (ii) re-fitting V1 and V2 to the simulated observations, and (iii) forming the corresponding value of the test statistic T. The procedure is repeated a total of 200 times and the observed significance level (or p value) is approximated by the proportion of occurrences the simulated value of T exceeds the value for the original data (T=7170).

A histogram of the values of T generated by this bootstrap procedure is shown in Fig. 9 along with the observed value. In this case, none of these values exceeds the observed value, so model V1 can be rejected in favor of model V2.

3.3. Consistency with prior estimates

A question of geochemical interest is whether the rate parameters ($k_1, k_{-1}, \beta_{-1}, w$) that are obtained from the fit of model V2 to GT11-22 data vary within plausible ranges. To address this question, we compare the vertical variations of ($k_1, k_{-1}, \beta_{-1}, w$) obtained from the fit with the prior estimates of these parameters (Fig. 10). The posterior estimates of k_1, k_{-1}, β_{-1}, and w are all within two standard deviations of the prior estimates, indicating that the rate parameters inferred from the fit of model V2 to GT11-22 data are consistent with prior knowledge. The most significant differences between the prior and posterior values occur for the particle sinking speed (Fig. 10d), a result elaborated upon below (Section 4.2). Note also the dramatic reduction in the prior uncertainties in ($k_1, k_{-1}, \beta_{-1}, w$) that results from
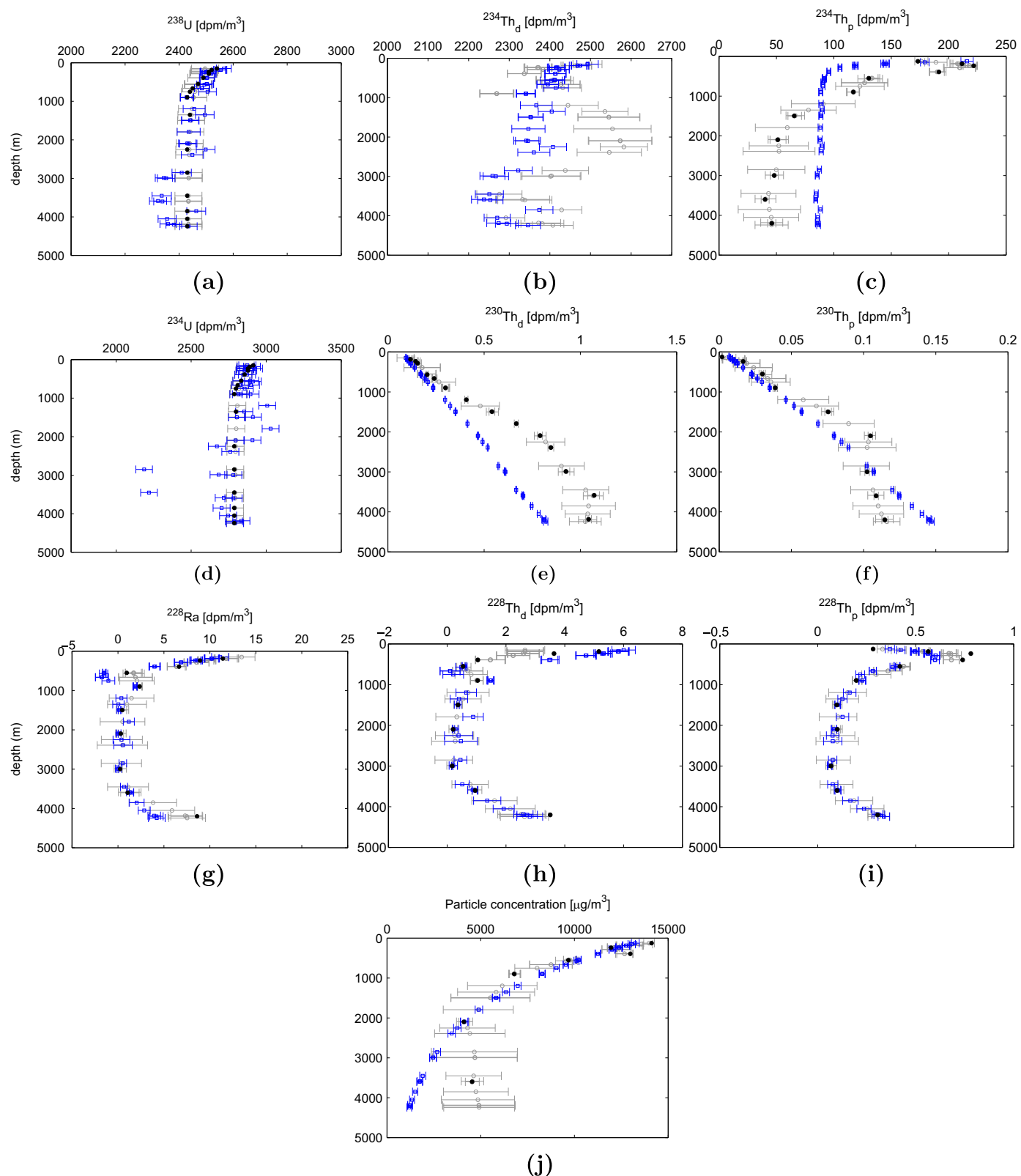
Fig. 7. Radiochemical activities and particle concentrations at station GT11-22. The black circles are the measured values, the open circles are the interpolated values, and the blue squares are the fitted values for model V1. Horizontal bars represent ± 1 standard deviation.

the combination of model V2 with station GT11-22 data (Fig. 10).

4. Discussion

Our results indicate that a model with depth-dependent rate

parameters provides a significantly better description of particle concentration and thorium activity data at station GT11-22 than a model with uniform rate parameters. While non-negative rate parameters are obtained for both model V1 and V2, there is a disconcerting feature in both solutions: ^{228}Ra values inferred by
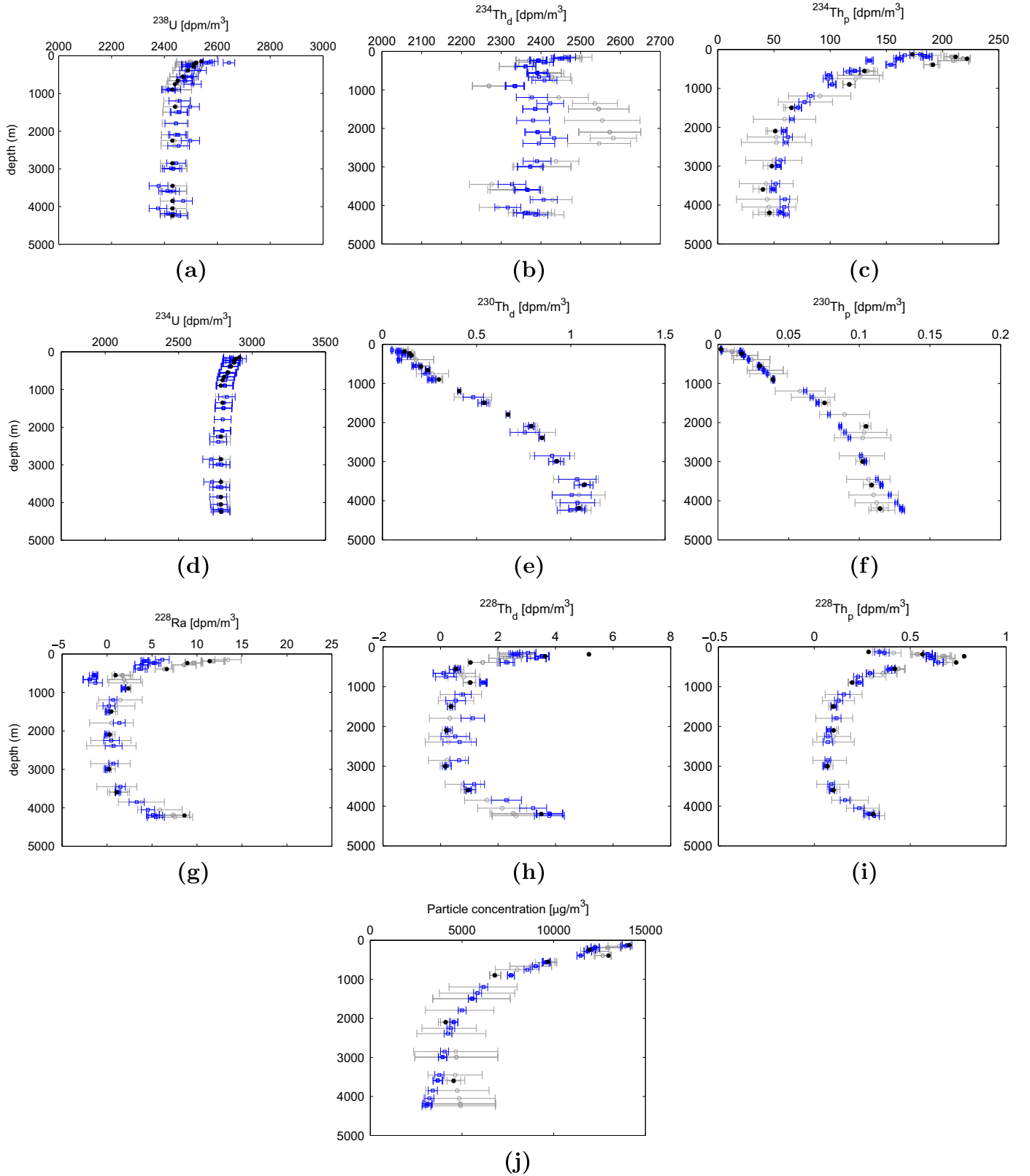
Fig. 8. Same as Fig. 7, but for model V2.

inversion near 500 m are negative, which is nonsensical (Figs. 7 and 8). These values differ from 0 dpm m^{-3} by more than one standard deviation. While these negative values are evidence that the model is not consistent with the data, we think that by themselves they do not warrant definitive rejection of the model. In testing model V1 and V2, any solution elements that deviate significantly from the

data, not only negative values, should be interpreted as a failure to explain the entire data set. Generally, one does not definitively reject a model because a few observations cannot be replicated. Indeed, the model may still replicate most of the observations, and thus provide a useful (albeit clearly not exact) description. The negative ^{228}Ra values are a reflection of inconsistencies between the data and

Table 2
Measures of goodness of fit of model V1 and V2 to station GT11-22 data[a].

	$\sigma_M^2 = 0.5\sigma_d^2$	$\sigma_M^2 = \sigma_d^2$	$\sigma_M^2 = 0.25\sigma_d^2$	$l_z = 2000$ m	$l_z = 500$ m
ϕ for V1	0.54	0.55	0.52	0.52	0.55
ϕ for V2	0.74	0.76	0.73	0.73	0.78
B for V1	−1.91	−1.86	−2.00	−1.96	−1.89
B for V2	−0.45	−0.40	−0.53	−0.49	−0.41

[a] For each listed σ_M^2, $l_z = 1000$ m. For each listed $l_z, \sigma_M^2 = 0.5\sigma_d^2$
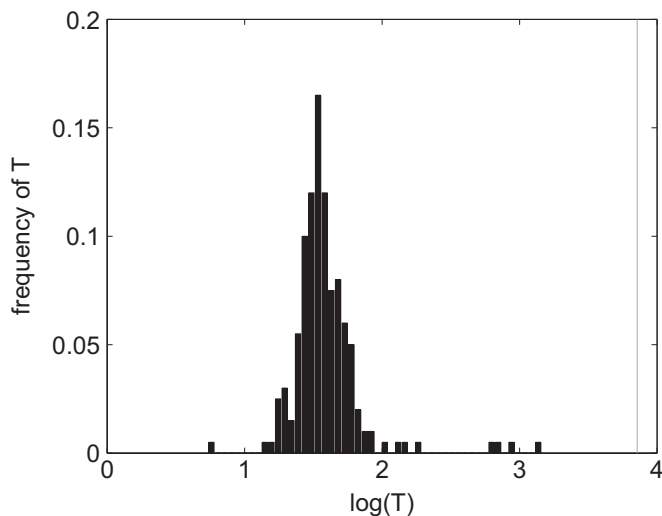

Fig. 9. Histogram of the frequency of the test statistic T obtained from the boot-strap. The grey line shows the value of T obtained from our reference solution (Section 3). The abscissa is the base-10 logarithm of the test statistic. Note that two negative values of T were found (-67 and -905), which are not shown in the figure.

the model, which should be understood before a decision is made about the plausibility of the model.

The importance of using a data set consisting of multiple thorium isotope and particle measurements is highlighted in Fig. 11. In this figure, we consider the more usual situation where data for only one Th isotope (here ^{230}Th) are available. In order to test model V1, the ^{230}Th$_d$ and ^{230}Th$_p$ data would be individually regressed linearly versus depth (Nozaki and Nakanishi, 1985; Edmonds et al., 1998; Okubo et al., 2012) (here a weighted least squares regression is used). The ^{230}Th$_p$ values estimated by regression are comparable with those estimated from the entire data set (compare solid line with grey circles in Fig. 11b). In contrast, the ^{230}Th$_d$ values from the regression are systematically larger than those inferred from the entire data set and much closer to the measurements (Fig. 11a). With only ^{230}Th data available, one might perhaps conclude that model V1 provides an adequate description of the data, which contrasts with the conclusion drawn from the multiple thorium isotope and particle concentration data set. This result illustrates the pitfall of using data for only one Th isotope when making inferences about the appropriateness of a Th cycling model.

4.1. Robustness of the test

4.1.1. Sensitivity to vertical smoothing

In Section 3, we tested model V2 using a smoothing parameter $\gamma = 1$. In order to document the effect of γ on our results, we fit model V2 to GT11-22 data (interpolated values obtained using $\sigma_M^2 = 0.5\sigma_d^2$ and $l_z = 1000$ m) using $\gamma = 0.01$ or $\gamma = 100$. For $\gamma = 0.01$, a solution is found after 66 iterations and the model equations are satisfied to the third order. For $\gamma = 100$, a solution is found after 8 iterations and the model equations are also satisfied to the third

order. When $\gamma = 0.01$, the fraction of normalized residuals less than 2 in absolute magnitude (ϕ) reaches 0.86, and the bias (B) shrinks to -0.27. When $\gamma = 100$, $\phi = 0.62$ and $B = -0.60$. Thus decreasing γ improves the fit of model V2 to the data, though in each case model V2 displays a better fit to the data than model V1 (see Table 3). The resulting vertical profiles of $(k_1, k_{-1}, \beta_{-1}, w)$ are compared in Fig. 12. As expected, the posterior variances in the rate parameters are larger when γ is smaller. Moreover, some β_{-1} and w values are negative if $\gamma = 0.01$. The intermediate value of $\gamma = 1$ provides the rate parameters some ability to vary with depth while preventing them from taking on negative values.

4.1.2. Sensitivity to initial estimates

In Section 3, our initial estimate $\hat{\mathbf{x}}_{k=0}$ was constructed so as to satisfy the measurements and the interpolation assumptions, i.e., $\hat{\mathbf{x}}_{k=0} = \mathbf{x}_0$. However, due to the nonlinearity of $\mathbf{f}(\mathbf{x})$, the ATI may converge to a solution that depends on $\hat{\mathbf{x}}_{k=0}$ (Tarantola and Valette, 1982). In particular, with $\mathbf{f}(\mathbf{x})$ being nonlinear, initial estimates of $\mathbf{x}$ that are far from the "true" solution may not lead to this solution but to a secondary minimum of J. Here we examine whether our results hold for a different initial estimate of the state vector, i.e. $\hat{\mathbf{x}}_{k=0} \neq \mathbf{x}_0$. Specifically, $\hat{\mathbf{x}}_{k=0}$ is constructed so as to satisfy the model equations perfectly: the parent activities (^{234}U,^{238}U,^{228}Ra), the boundary values of ^{228,230,234}Th$_p$ and P, and the rate parameters are equal to their prior values as in Section 3, but the other elements of $\hat{\mathbf{x}}_{k=0}$ (^{228,230,234}Th$_{d, p}$ and P at all depths save at the boundary point) are obtained as the solution of the model with these prior values.

We find that the results of the inversions for the two different estimates $\hat{\mathbf{x}}_{k=0}$ are very similar (Table 3). The ATI converges to a stable solution after 12 iterations and all model equations are satisfied to at least the third order. Model V2 provides a superior fit to the data ($0.73 \leq \phi \leq 0.74$) compared to model V1 ($\phi = 0.54$). The bias of the fit is also similar between both inversions for model V2 ($-0.45 \leq B \leq -0.4$) and both inversions for model V1 ($B = -1.91$). Thus, our test of models V1 and V2 does not depend on whether the initial state estimate satisfies the entire set of prior values, or only a fraction of the prior values and the model equations. This result is encouraging, although we cannot rule out that other plausible choices of $\hat{\mathbf{x}}_{k=0}$ would lead to different results.

4.1.3. Sensitivity to bulk particle activities

Our observational estimates of bulk particulate ^{234,230,228}Th assumed a ratio between large and small particulate Th activities of 0.19 (see Section 2.4). This value is large compared to the ^{234}Th$_{p, l}/^{234}$Th$_{p, s}$ ratio of 0.07 found by Buesseler et al. (2001) in the Southern Ocean. In order to test the effects of a smaller ratio, we repeat our inversion using bulk particulate Th data based on a large to small particulate Th activity of 0.07 (Buesseler et al., 2001). We find that, in this case, the model equations are satisfied to the third order, and the objective function again converges after 14 iterations. The results are very similar to those of our reference solution (Table 3).

4.1.4. Sensitivity to lithogenic sources

Our model does not consider the contribution of a lithogenic source to ^{230}Th$_p$. In order to test the sensitivity of our results to the inclusion of this source, we repeat our inversion by correcting ^{230}Th$_p$ data for a contribution from lithogenic material (Section 2.5). In this case, we find that the model equations are satisfied to the third order, and the objective function converges after 15 iterations. No notable difference between these results and those from the reference inversion occurs (Table 3). Despite the relatively large (>30%) contribution to ^{230}Th$_p$ from lithogenic particles in the upper 500 m, the solution is insensitive to this correction, presumably because the lithogenic source is small compared to other sources and sinks of ^{230}Th$_p$.
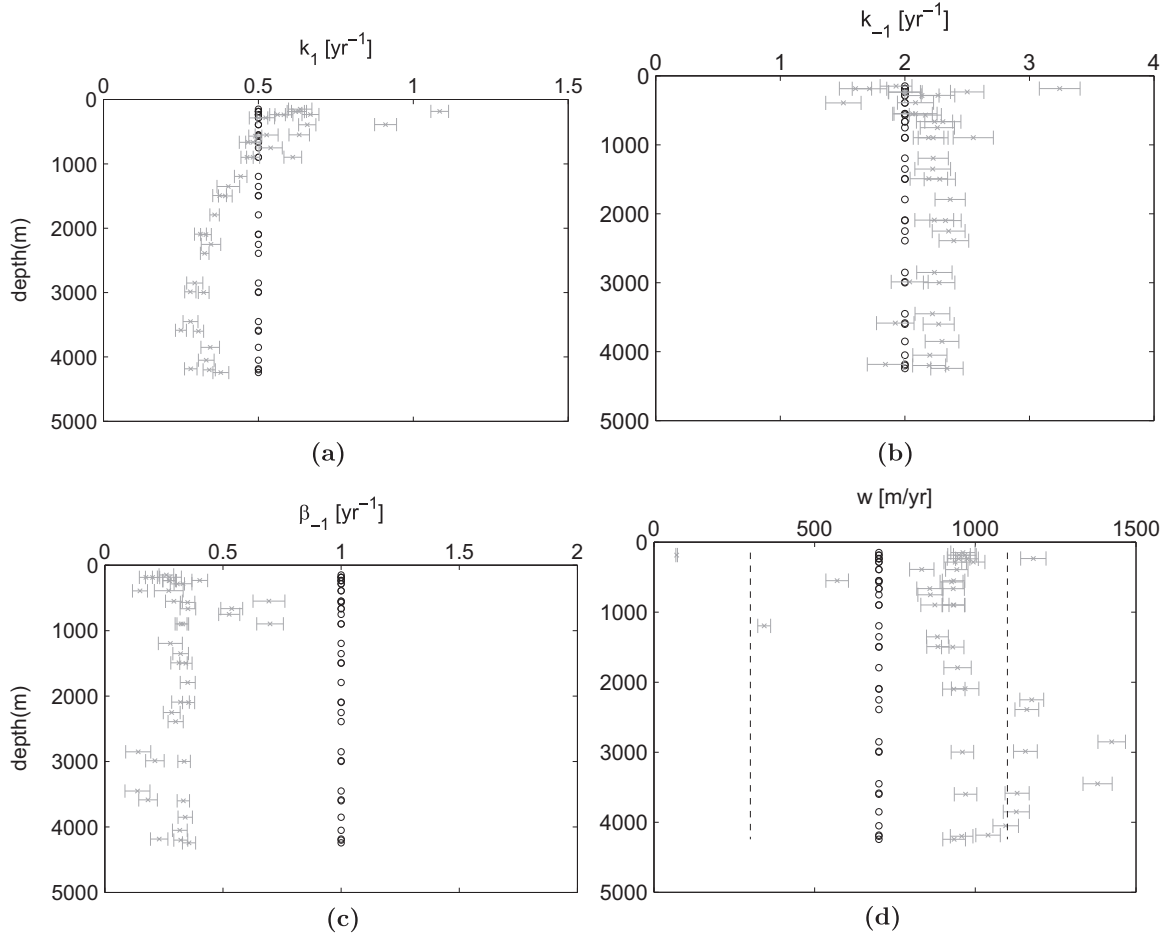
Fig. 10. Rate parameters of Th and particle cycling at station GT11-22 as inferred from the combination of data with model V2. The open circles are the prior values ($k_1 = 0.5 \pm 5$ yr^{-1}, $k_{-1} = 2 \pm 5$ yr^{-1}, $\beta_1 = 1 \pm 10$ yr^{-1}, $w = 700 \pm 400$ m yr^{-1}). The vertical dashed lines in (d) show the range [300–1100] m yr^{-1} for the prior estimate of the particle sinking speed. The grey crosses are the posterior estimates ± 1 standard deviation (obtained by inversion). For comparison, the rate parameters inferred from the combination of data with model V1 are $k_1 = 0.49 \pm 0.01$ yr^{-1}, $k_{-1} = 2.11 \pm 0.07$ yr^{-1}, $\beta_1 = 0.46 \pm 0.02$ yr^{-1}, $w = 725 \pm 7$ m yr^{-1}.
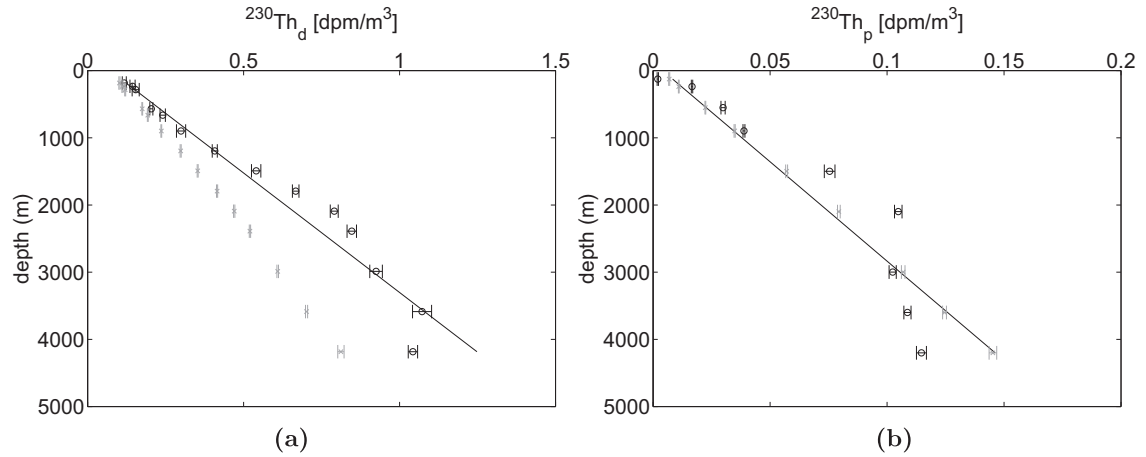

Fig. 11. The left panel shows the ^{230}Th$_d$ measurements at station GT11-22 (open circles), the posterior estimates of ^{230}Th$_d$ from the fit of model V1 (grey crosses) to the entire data set (^{234,238}U,^{228,230,234}Th$_{d, p}$,P), and the line from fit of model V1 to only dissolved ^{230}Th data (derived from weighted least squares regression of ^{230}Th$_d$ with depth). Horizontal bars are ± 1 standard deviation. The right panel is the same as the left panel, but for ^{230}Th$_p$.

4.1.5. Sensitivity to filtering bias

Finally, we consider the effects of a potential bias due to the filters chosen to extract Th isotopes. Maiti et al. (2012) found no significant differences in ^{234}Th activities between different filter types and pore sizes (between 0.2 and 0.8 μm), except for the quartz filters: the ^{234}Th activities measured on QMA filters were found to be 10% to 20% higher than those measured on Supor filters. The higher activities on QMA filters were attributed mainly to sorption (Maiti et al., 2012). In order to test a potential bias due to ^{228,234}Th sorption on QMA filters, we repeat our inversions by reducing the particulate ^{234}Th and ^{228}Th data values by 20%. In this case, the model equations are satisfied to the third order and the

Table 3
Measures of goodness of fit of model V1 and V2 to GT11-22 data for different initial estimate $\boldsymbol{x}_{k=0}$.

	'Reference' $\hat{\boldsymbol{x}}_{k=0}$	Model-based $\hat{\boldsymbol{x}}_{k=0}$	$Th_{p,l}/Th_{p,s} = 0.07$	Corrected ^{230}Th[a]	QMA bias 20%
ϕ for V1	0.54	0.54	0.53	0.53	0.55
ϕ for V2	0.74	0.73	0.73	0.73	0.76
B for V1	-1.91	-1.91	-1.85	-1.84	-1.64
B for V2	-0.45	-0.40	-0.49	-0.46	-0.38

[a] Measured ^{230}Th$_{d,p}$ corrected for lithogenic ^{230}Th.
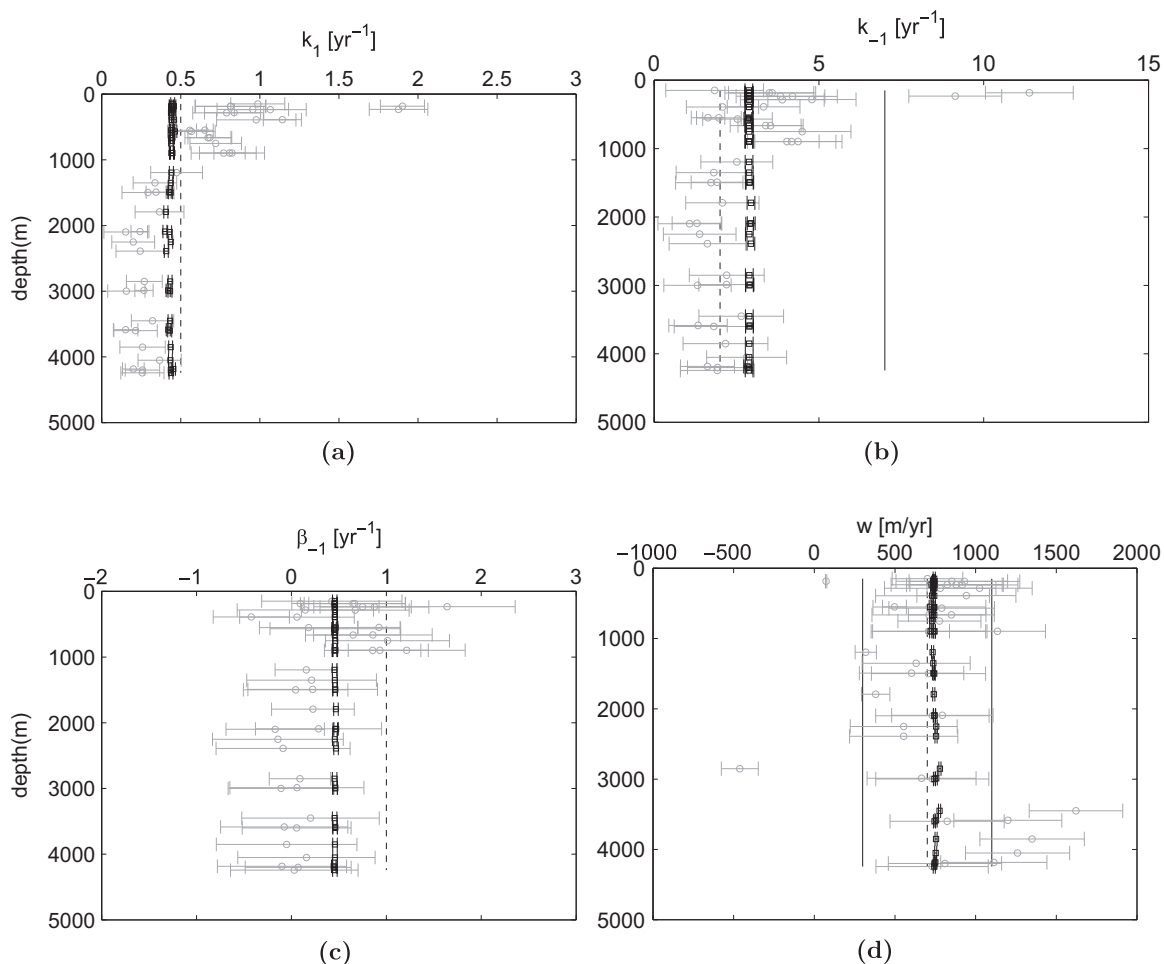
Fig. 12. Rate parameters of Th and particle cycling at station GT11-22 as inferred from the combination of data with model V2. The vertical dashed lines are the prior estimates, and the posterior estimates for $\gamma=0.01$ and $\gamma=100$ are represented by open grey circles and black squares, respectively. Horizontal bars are $\pm$ 1 standard deviation. The solid lines show the range [value $\pm$ one standard deviation] for the prior estimates.

objective function converges after 14 iterations. The values of ϕ and B are close to those of our reference solution (Table 3), suggesting our results are not very sensitive to a potential bias due to the use of different types of filters.

4.1.6. Kolmogorov-Smirnov test

In order to further test whether our results are robust against the changes discussed in Sections 4.1.2–4.1.5, we employ a Kolmogorov-Smirnov test (Appendix B). The tests show that these changes do not significantly alter the results compared to those of our reference solution (Section 3).

4.2. Implications for oceanic Th geochemistry

4.2.1. Effect of particle concentration

In this section, we examine the roles of adsorption (k_1), desorption (k_{-1}), and remineralization (β_{-1}) in the fit of model V2 to GT11-22

data. For simplicity we consider a single parameter, $K = k_1/(k_{-1} + \beta_{-1})$. Thus, a value of $K < 1$, for example, would imply that the specific rate at which Th attaches to particles is smaller than those at which it is released from particles by desorption and remineralization. Interestingly, the vertical profile of K in our reference solution (Section 3) shows a decrease with depth in the upper 2000 m and relatively uniform values below (Fig. 13a). Using data from the Guatemala and Panama Basins, Bacon and Anderson (1982) estimated that the k_1/k_{-1} ratio ranged from 0.078 to 0.462, where their k_{-1} included both remineralization and desorption. These values are consistent with our estimates of K at station GT11-22. However, the k_1/k_{-1} ratio of Bacon and Anderson (1982) did not show similar variability with depth across stations, so it is unclear whether the profile of K derived here (Fig. 13a) is consistent with their findings.

We find a higher K value in the upper 2000 m, mainly because k_1 is enhanced in these waters (Fig. 9). A potential cause of the
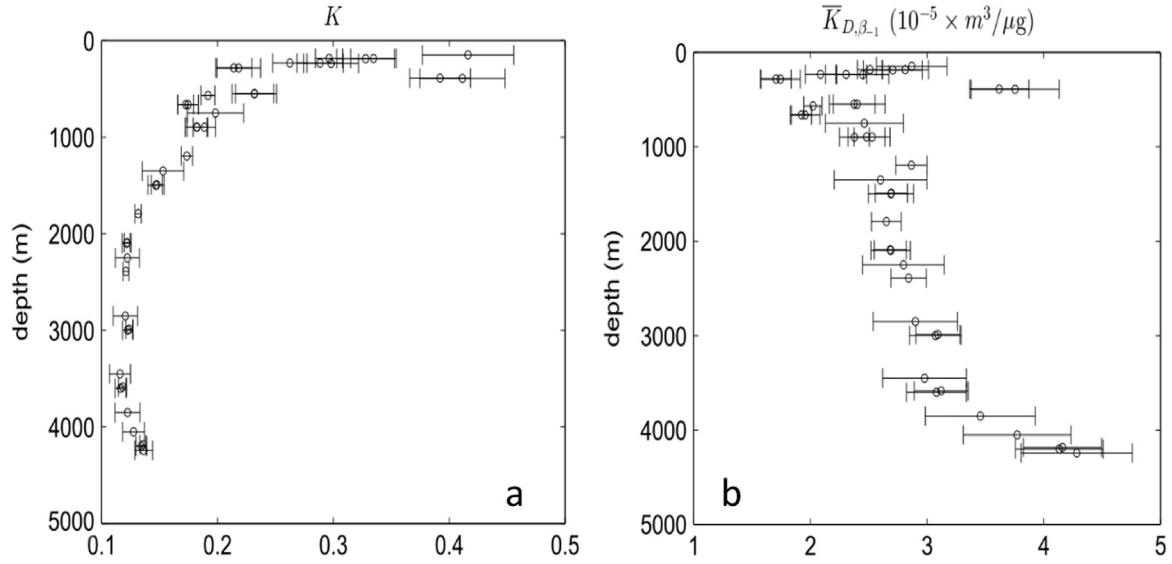
Fig. 13. Profiles of $K = k_1/(k_{-1} + \beta_{-1})$ (a) and $\overline{K}_{D,\beta_{-1}} = K/P$ (b) at station GT11-22, as inferred from the combination of data with model V2. The horizontal bars show the errors (one standard deviation) derived from propagating the posterior errors of k_1, k_{-1}, β_{-1} (and P for $\overline{K}_{D,\beta_{-1}}$), with due regard for the error covariances.
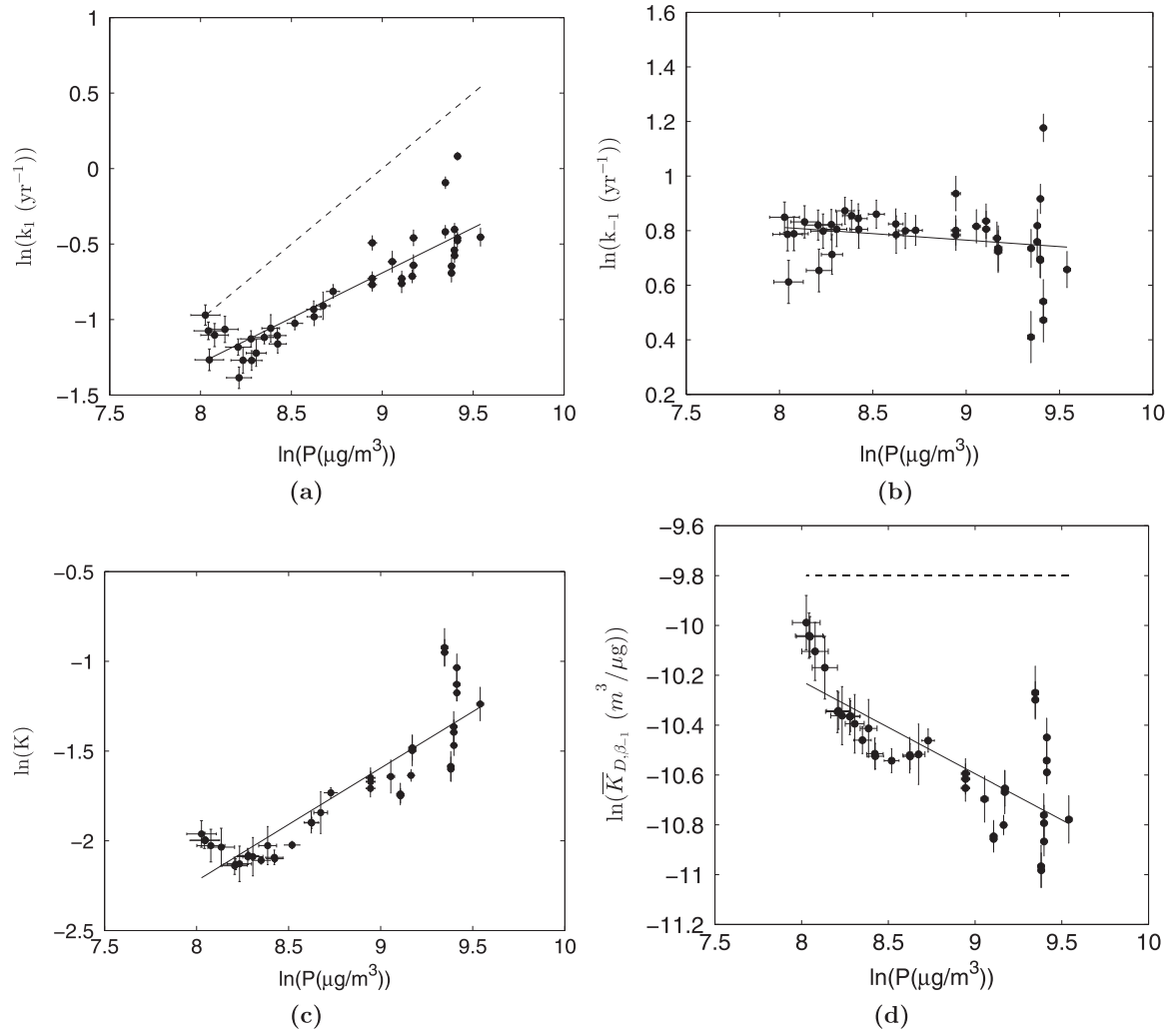

Fig. 14. Variation of k_1 (a), k_{-1} (b), $K = k_1/(k_{-1} + \beta_{-1})$ (c), and $\overline{K}_{D,\beta_{-1}} = K/P$ (d) with particle concentration, as inferred from inversion of station GT11-22 data. Horizontal and vertical bars show ± 1 standard deviation. In each panel, the solid line is the ordinary least squares fit. The slopes of these lines are (a) 0.81 ± 0.06, (b) 0.06 ± 0.03 (c) 0.73 ± 0.06, and (d) -0.28 ± 0.06. In panels (a) and (d), the dashed line represents the slope expected in the absence of a particle concentration effect (the slope of this dashed line is 1 in panel a, and 0 in panel d).

increased adsorption rate constant in the upper 2000 m is the higher particle concentration in this region of the water column, because of the increase in the number of surface sites available for attachment (Honeyman et al., 1988). We assess the strength of the association between k_1 and P (Fig. 14a), as well as between K and P (Fig. 14b), using the Kendall tau (τ) rank correlation coefficient (Kendall and Gibbons, 1990). This coefficient ranges between -1 and 1, where a value of 1 (-1) implies a perfect positive (negative) monotonic relationship between k_1 (or K) and P. We find that $\tau = 0.73$ ($p < 0.01$) for the relationship between k_1 and P, and $\tau = 0.70$ ($p < 0.01$) for the relationship between K and P (the Pearson correlation coefficient for both of these relationships amount to $r = 0.89$). Thus both k_1 and K increase significantly with P.

Honeyman et al. (1988) and Honeyman and Santschi (1989) have calculated an equilibrium distribution coefficient, $\overline{K}_D = k_1/(k_{-1}P)$ to describe the affinity of trace metals for particles. Echoing previous studies, Honeyman et al. (1988) found that $\overline{K}_D$ decreases with increasing particle concentration, a phenomenon referred to as the "particle concentration effect". According to these authors, one potential cause for this effect is that the rate of adsorption of trace metals onto filterable particles depends on the rate of coagulation of colloidal ($<0.8\,\mu m$) particles. They showed that $\overline{K}_D$ should decrease with P, even though k_1 increases with particle concentration, because $\overline{K}_D$ varies explicitly as P^{-1} while k_1 has a power law dependence with particle concentration, $k_1 = k_{1,c}P^b$, where $k_{1,c}$ is constant and $b < 1$.

We examine the possibility of a particle concentration effect at station GT11-22 from the values of $\overline{K}_{D,\beta_{-1}} = k_1/((k_{-1} + \beta_{-1})P)$ obtained from the fit of model V2 to the data gathered at that station. The profile of $\overline{K}_{D,\beta_{-1}}$ shows a general increase with depth (Fig. 13b). Hayes et al., (2015a) estimated $K_D = A_p/(A_dP)$ from ^{230}Th and filtered particle concentration data from the GA03 transect (Eq. (3b)) shows that A_p/A_d equals $k_1/(k_{-1} + \beta_{-1})$ if sinking and radioactive decay are neglected). Their method involved dividing ^{230}Th adsorbed onto particles by ^{230}Th in the dissolved phase and normalizing this ratio to the filtered particulate matter concentration ($>0.8\,\mu m$). Our values for $\overline{K}_{D,\beta_{-1}}$, between 1.5×10^{-5} and $5 \times 10^{-5}\,m^3\,\mu g^{-1}$, are within the range found by Hayes et al., (2015a) below 500 m, from about 1×10^{-5} to about $1 \times 10^{-4}\,m^3\,\mu g^{-1}$. Plotting $\ln(\overline{K}_{D,\beta_{-1}})$ against $\ln(P)$ suggests that, in general, $\overline{K}_{D,\beta_{-1}}$ decreases with P (Fig. 14d). The rank correlation between $\ln(\overline{K}_{D,\beta_{-1}})$ and $\ln(P)$ amounts to $\tau = -0.62$ with $p < 0.01$ ($r = -0.75$), which indicates a significant negative monotonic relationship between both variables and hence the possibility of a particle concentration effect. Note that below about 3500 m, the vertical gradient of $\overline{K}_{D,\beta_{-1}}$ is particularly large. However, this feature is due at least partly to the decrease in the estimated particle concentrations below 3500 m, which is not observed (Fig. 8).

If a particle concentration effect exists, k_1 should vary as P^b, where b is less than 1 (see dashed line in Fig. 14a). Conversely, in the absence of such an effect, $\overline{K}_{D,\beta_{-1}}$ should be independent of particle concentration (see dashed line in Fig. 14d). A least-squares fit of $\ln(k_1)$ vs. $\ln(P)$ yields a slope of 0.81 ± 0.06. This contrasts with the slope obtained by Honeyman et al. (1988) of 0.51–0.58 from field data spanning a much larger particle concentration range from $O(10^4\,\mu g\,m^{-3})$ to $O(10^{12}\,\mu g\,m^{-3})$. For the regression of $\ln(\overline{K}_{D,\beta_{-1}})$ against $\ln(P)$, we obtain a slope of -0.28 ± 0.06, smaller in magnitude than the slope of -0.42 found by Honeyman et al. (1988) from the same field data used to obtain their $\ln(k_1)$ vs. $\ln(P)$ slope. These results suggest that the particle concentration effect we obtain from our analysis of station GT11-22 data is not as strong as that reported by Honeyman et al. (1988) for a much larger particle concentration range. This discrepancy may arise because the particle concentrations reported at station GT11-22 are lower than those considered by Honeyman et al. (1988). Honeyman and Santschi (1989) found that $\overline{K}_D$ appears independent of particle concentration below

$10^5\,\mu g\,m^{-3}$, a value larger than P at any depth investigated here. Interestingly, using ^{230}Th activity and particle concentration data across the entire North Atlantic section, Hayes et al., (2015a) found a much larger slope of $\log_{10}(K_D)$ vs. $\log_{10}(P)$ of -0.66 ($r^2 = 0.53$). Such a discrepancy may be due to station GT11-22 being an oligotrophic site with low colloidal concentrations relative to stations closer to the margins. Nevertheless, our findings suggest that a particle concentration effect does remain present at this station, albeit reduced compared to the one found at higher particle concentrations.

Bacon and Anderson (1982) reported that k_{-1} does not depend on particle concentration from data collected in the Panama and Guatemala Basins. We test whether k_{-1} depends on particle concentration according to our analysis of GT11-22 data. We find that for the relationship between $\ln(k_{-1})$ and $\ln(P)$, $\tau = -0.18$ ($p = 0.11$) and the slope of the least squares fit is 0.06 ± 0.03 ($r = -0.19$). Thus, we find no significant evidence that P affects k_{-1}, consistent with Bacon and Anderson (1982).

4.2.2. Vertical variation in particle settling speed

In this section, we discuss the profile of particle sinking speed obtained from the fit of model V2 to GT11-22 data. Particle concentration in model V2 shows a decrease below 2000 m that is not as pronounced as in model V1. Associated with this feature is the inference of relatively large particle settling speeds below 2000 m. The particle sinking term can be either a loss or a source in the particle equation (Eq. (3c)). For example, if there are more particles at the depth above a grid point than at the depth of the grid point, that grid point will "gain" particles from sinking. In this case, increasing the sinking velocity tends to increase the particle concentration and to better offset the loss due to particle remineralization. As a result, particle concentration in deep water is higher in model V2 compared to model V1 (compare Fig. 7j to Fig. 8j).

It is difficult to determine possible mechanisms underlying the vertical variation in our particle sinking speed profile, in particular because our model does not discriminate between large and small particles. One of the most noticeable features in this profile is an apparent increase in sinking speed below 2000 m. One potential cause for the apparent increase in particle sinking speed is a local increase in the rate of aggregation of suspended particles, resulting in an increase in large, more quickly sinking particles and hence in bulk w. However, this appears unlikely given the nearly constant partitioning of particles between the small and large size fractions below 2000 m at station GT11-22 (Lam et al., 2015). The apparent increase in particle sinking speed may reflect a bias due to the exclusion of other processes that could increase particle concentration below 2000 m, such as lateral transport of suspended particles.

Below 2000 m, the particle sinking speed inferred by inversion exhibits significant variability on short vertical scales (Fig. 10). Interestingly, similar variability is not apparent in the inferred vertical profiles of the parent isotope activities, Th isotope activities, and particle concentration. Below 2000 m, the particle sinking term is a minor term in the balance of the particulate Th isotopes (Section 4.3), except for ^{228}Th$_p$. Speculatively, the large variability of w at small vertical scales would be due to the small vertical gradients of particulate ^{228}Th$_p$ between about 2000 and 3500 m: small changes in these gradients would require large changes in w to achieve a balance between the particulate ^{228}Th$_p$ sources and sinks at different levels within this depth interval. Whereas further inversions may help to isolate the specific measurements that are responsible for the inference of a large variability of w below 2000 m, such effort is beyond the scope of this study.

To our knowledge, there are no reported depth-varying estimates of the sinking speed of bulk particles (small + large) in the current literature. Armstrong et al. (2009) and Lee et al. (2009) collected sinking particles using indented rotating-sphere settling velocity (IRS-

SV) traps placed at various depths at a location in the northwestern Mediterranean Sea. These traps have the ability to sort the mass flux density of particles into sinking speed bins. The mass flux density is defined as the mass of any constituent per square meter of trap area, integrated over the trap deployment time and divided by $\log_{10}(SV_{max}/SV_{min})$, where $SV_{max}(SV_{min})$ is the maximum (minimum) particle settling speed in a given SV range. Armstrong et al. (2009) and Lee et al. (2009) found that, at all depths, (i) the majority of the mass flux density of particles occurs within a rapidly sinking (200–500 m d^{-1}) speed interval, and (ii) the mass flux density presents an exponential "tail" within a much slower (0.68–2.7 m d^{-1}) sinking speed interval. Closer to station GT11-22, Alonso-González et al. (2010) conducted a study south of the Canary Islands using IRS-SV traps placed at a depth of 260 m. They found that the mass flux density was highest in the low sinking speed range (0.7–11 m d^{-1}), which overlaps with the range of sinking speeds obtained from the fit of model V2 to GT11-22 data (0.19–3.86 m d^{-1}). Therefore, it could be concluded that the vast majority of particles below 125 m at station GT11-22 settle very slowly. However, comparison to our study is difficult. Whereas Armstrong et al. (2009), Lee et al. (2009), and Alonso-González et al. (2010) consider particles within specific sinking speed ranges, the sinking speeds reported here are average values for the bulk particle concentration (all particles) at a given depth. The sinking speeds of the different particles may vary greatly, making the interpretation of our estimated sinking speeds difficult. Therefore, caution must be applied when comparing our bulk particle sinking speeds to those obtained from sediment or settling velocity traps.

4.3. Diagnosis of Th isotope budgets

In this section, we examine the budget of each Th isotope at station GT11-22, as determined by inversion of the particle and radiochemical data. The different terms of the budget are, for each Th isotope, the adsorption flux ($k_1 A_d$), the desorption flux ($k_{-1} A_p$), the remineralization flux ($\beta_{-1} A_p$), the particle sinking flux ($w \partial A_p/\partial z$), the decay fluxes ($\lambda A_d$, λA_p), and the production flux (λA_π). Since our estimation of the flux terms accounts for the data uncertainties but not for the model uncertainties, it should only be considered as suggestive.

4.3.1. ^{234}Th

The dominant terms in the ^{234}Th$_d$ budget (Fig. 15) are the production and decay terms. These terms are the largest because ^{234}Th$_d$ and ^{238}U are one order of magnitude larger than ^{234}Th$_p$, and the decay constant for ^{234}Th is about one order of magnitude larger than k_1, k_{-1}, and β_{-1}. For the ^{234}Th$_p$ budget, the first-order terms are the adsorption flux and radioactive decay. The adsorption term dominates because it includes ^{234}Th$_d$, and the decay term is the main loss because the decay constant is much larger than the other rate constants. The particle sinking term is particularly small below 800 m, where ^{234}Th$_p$ shows small vertical variations (Fig. 5). The average fluxes, taken by integrating the source and loss terms and dividing by the vertical extent of our domain (from 125 to 4243 m), are shown in Fig. 15a. To obtain kinetic measures in the budget, we calculate residence times by dividing the depth-averaged Th isotope activity by the dominant depth-averaged volumetric flux associated with that isotope. We find that the residence time with respect to radioactive production is 34 days for ^{234}Th$_d$, and the residence time with respect to adsorption is 29 days for ^{234}Th$_p$.

4.3.2. ^{228}Th

Unlike for ^{234}Th$_d$, the dominant terms in the ^{228}Th$_d$ budget vary with depth. Near the surface, radioactive production is the dominant source, and is balanced mostly by adsorption of ^{228}Th$_d$. However, throughout most of the water column, adsorption, decay,

desorption, and production are nearly equivalent in magnitude. Below 3500 m, adsorption and decay are comparable as losses of ^{228}Th$_d$, and production once again becomes the dominant source. This pattern is consistent with the vertical profile of ^{228}Ra, which has surface and deepwater maxima and is minimum near the middle of the water column. Thus production is highest in near-surface and deep waters. Near the surface, the adsorption term is larger than decay of ^{228}Th$_d$, even though both scale with ^{228}Th$_d$, because k_1 is highest in surface waters (Fig. 10).

The dominant terms in the ^{228}Th$_p$ budget similarly vary with depth. Near the shallowest depth, adsorption is the dominant source, balanced mostly by desorption. Near the surface, the particle sinking flux is a loss term for ^{228}Th$_p$, but becomes a source equivalent in magnitude to adsorption below about 500 m. Below about 3500 m, ^{228}Th$_p$ is lost in about equal measure through particle sinking and desorption, and is gained solely through adsorption. We show the average fluxes for ^{228}Th$_{d, p}$ in Fig. 16a. The residence time of ^{228}Th$_d$ and ^{228}Th$_p$ with respect to adsorption is 891 days (2.44 yr) and 125 days, respectively.

4.3.3. ^{230}Th

Since the radioactive decay constant for ^{230}Th is about 5 orders of magnitude smaller than the rate parameters k_1, k_{-1}, and β_{-1}, production and decay generally no longer dominate the budget for the dissolved and particulate phases. Instead, desorption is the first-order source of ^{230}Th$_d$ and adsorption is the first-order loss, with production and remineralization being second-order gains except nearest to the surface. The primary mechanisms influencing ^{230}Th$_p$ are also adsorption and desorption, with remineralization and sinking being generally losses of second-order importance. We show the average fluxes for ^{230}Th$_{d, p}$ in Fig. 17a. The residence time of ^{230}Th$_d$ and ^{230}Th$_p$ with respect to adsorption is 1090 days (2.98 yr) and 130 days, respectively.

4.4. Interpretation of particle and Th isotope residuals

4.4.1. Model with uniform rate parameters

The values of ^{234}Th$_d$ estimated from the fit of model V1 to GT11-22 data show vertical variations associated with vertical variations in ^{238}U (Fig. 7). Some of the ^{238}U values inferred from the fit differ from prior values estimated from salinity by more than one standard deviation. These values seem to stem from the attempt by the algorithm to produce the best fit to the ^{234}Th$_d$ data: since rate parameters cannot vary with depth in model V1, the algorithm allows the parent isotope to change in order to fit the daughter. In any case, it is clear that model V1 cannot fit uranium and thorium activities very well (e.g. Fig. 7e), with the exception of ^{228}Th and ^{228}Ra. Unlike the ^{238,234}U estimates derived from salinity, ^{228}Ra measurements show consistent variability with depth (maxima in near surface and deep waters, minima at mid-depth), which is largely reflected in the ^{228}Th$_d$ and ^{228}Th$_p$ data. Therefore, whereas the algorithm produces ^{234,238}U values that deviate significantly from prior estimates, such large deviations from the prior estimates are generally not as necessary for ^{228}Ra to reach consistency with the model. Finally, the particle concentrations inferred by inversion show an exponential decrease with depth, in contrast to the data which shows a slight increase below 2000 m. Below this depth, model V1 is unable to replicate the particle data within two standard deviations (Fig. 7).

4.4.2. Model with non-uniform rate parameters

Model V2 produces enhanced agreement with radiochemical and particle data from station GT11-22 (Fig. 8). This can be viewed most clearly by the much improved fit of model V2 to ^{234,238}U, ^{230}Th$_d$, and particle data. However, even allowing the rate parameters to vary with depth does not allow the model to fit the entire data set. In particular, ^{234}Th$_d$, ^{230}Th$_p$, and particle concentration contain regions
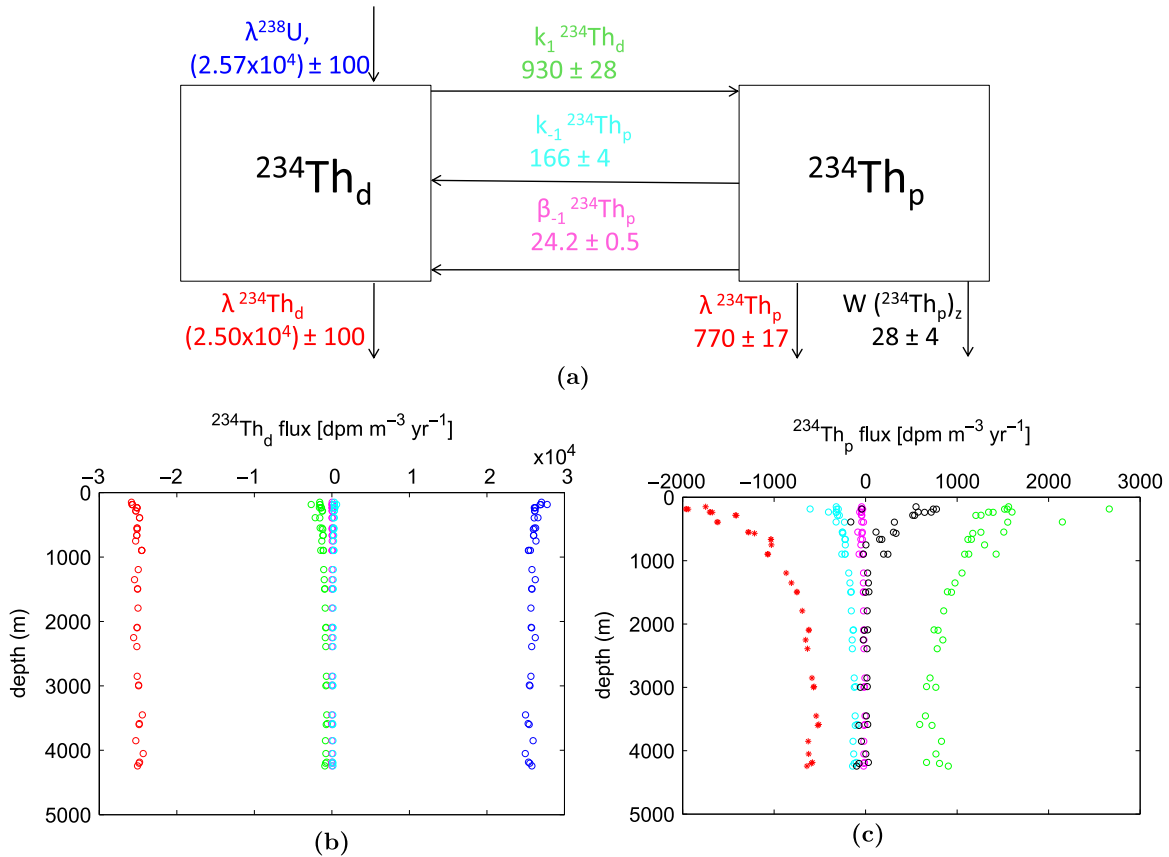
Fig. 15. Panel (a) shows the ^{234}Th budget at station GT11-22. The displayed values are vertical averages (125–4243 m) in dpm m^{-3} yr^{-1}. Panel (b) and (c) show the vertical distribution of the ^{234}Th fluxes. In all panels, red for radioactive decay, blue for radioactive production, green for adsorption, cyan for desorption, magenta for remineralization, and black for the sinking flux.

of relatively large normalized residuals (Fig. 8). The vertical variations in the ^{234}Th$_{tot}$ data (used to derive ^{234}Th$_d$) are large compared to those in the salinity-based estimates of ^{238}U (compare Fig. 5a with Fig. 5b). The half-life of ^{234}Th$_d$ (24.1 days) implies that processes responsible for departure from secular equilibrium should be characterized by a timescale of a few weeks or less. It is worthwhile to note that such departures from secular equilibrium in deep-water ^{234}Th$_{tot}$ are not unique to station GT11-22. Owens et al. (2015) have shown how ^{234}Th$_{tot}$ disequilibrium is prevalent in deep waters throughout the section. For instance, cross-over station GT11-24 (Fig. 1) exhibits ^{234}Th$_{tot}$ deficits, while station GT22-20 (the second station to the west of GT11-22; Fig. 1) exhibits ^{234}Th$_{tot}$ excess, like station GT11-22. While a subsurface excess in ^{234}Th$_{tot}$ relative to secular equilibrium may be explained by a deficit in ^{234}Th in the surface due to enhanced scavenging and subsequent remineralization of Th-laden particles just beneath the surface (Maiti et al., 2015), a mechanism for maintaining a ^{234}Th$_{tot}$ excess below 1000 m has yet to be elucidated. Therefore, the variations in ^{234}Th$_{d, tot}$ remain a confounding element of the GEOTRACES North Atlantic data set.

On the other hand, ^{230}Th appears more likely to be influenced by the transport of water masses. Due to its long half-life, ^{230}Th anomalies can be transported over large distances in the ocean, provided that these anomalies are not erased by the effects of particle scavenging and water mixing. For example, ventilation by ^{230}Th$_d$-poor water from the northern North Atlantic has been postulated to influence ^{230}Th in deep water in the North Atlantic (Moran et al., 1997; Vogler et al., 1998). Here, we examine the potential influence of two water masses, Upper Labrador Sea Water (ULSW) and Central Labrador Sea Water (CLSW), on the misfits of model V2 to ^{230}Th data for station GT11-22. Fig. 18 compares the normalized ^{230}Th$_d$ and ^{230}Th$_p$ residuals with the

estimated proportion of ULSW and CLSW at this station (Jenkins et al., 2015). Since LSW is characterized by low ^{230}Th$_d$ (Moran et al., 2002), an intrusion of LSW at station GT11-22 should be reflected in low ^{230}Th$_d$ activities between 1500 and 3000 m. Such an intrusion would also result in low ^{230}Th$_p$ if ^{230}Th$_d$ continuously undergoes reversible exchange in transit. However, the ^{230}Th$_d$ normalized residuals are only large (and negative) in the top 500 m, and do not show any systematic change below 1500 m, where Labrador Sea Waters are inferred to be present (Section 2.1). Therefore, it seems unlikely that the ^{230}Th$_{d, p}$ residuals arise from the omission of the effect of LSWs in the model. Other processes missing in model V2 must be responsible for the significant ^{230}Th$_{d, p}$ residuals (see Section 2.4 for model limitations).

Both model V1 and V2 underpredict particle concentrations compared to observations below 2000 m. Since our interpolation grid only extends down to 4243 m, only 2 measurements of particle concentration were considered in the data interpolation below 2000 m. Inspection of the entire particle concentration profile from 125 m to 4989 m (Fig. 19) confirms that particle concentration remained constant or increased slightly with depth below 2000 m, consistent with beam attenuation coefficient data at station GT11-22 (Anderson et al., 2013). Although a slight bottom nepheloid layer might have been present at station GT11-22, as was observed at other stations along the section (Lam et al., 2015), the particle residuals below 2000 m (Fig. 19) should probably not be interpreted as due to the omission of such a layer in the model. Another potential source of misfit of model V2 to particle concentration data is lateral transport of suspended particles (Alonso-González et al., 2010), although it is unclear whether there can be particle enriched waters moving laterally to station GT11-22 below 2000 m. McCartney et al. (1991) and Schmitz and McCartney
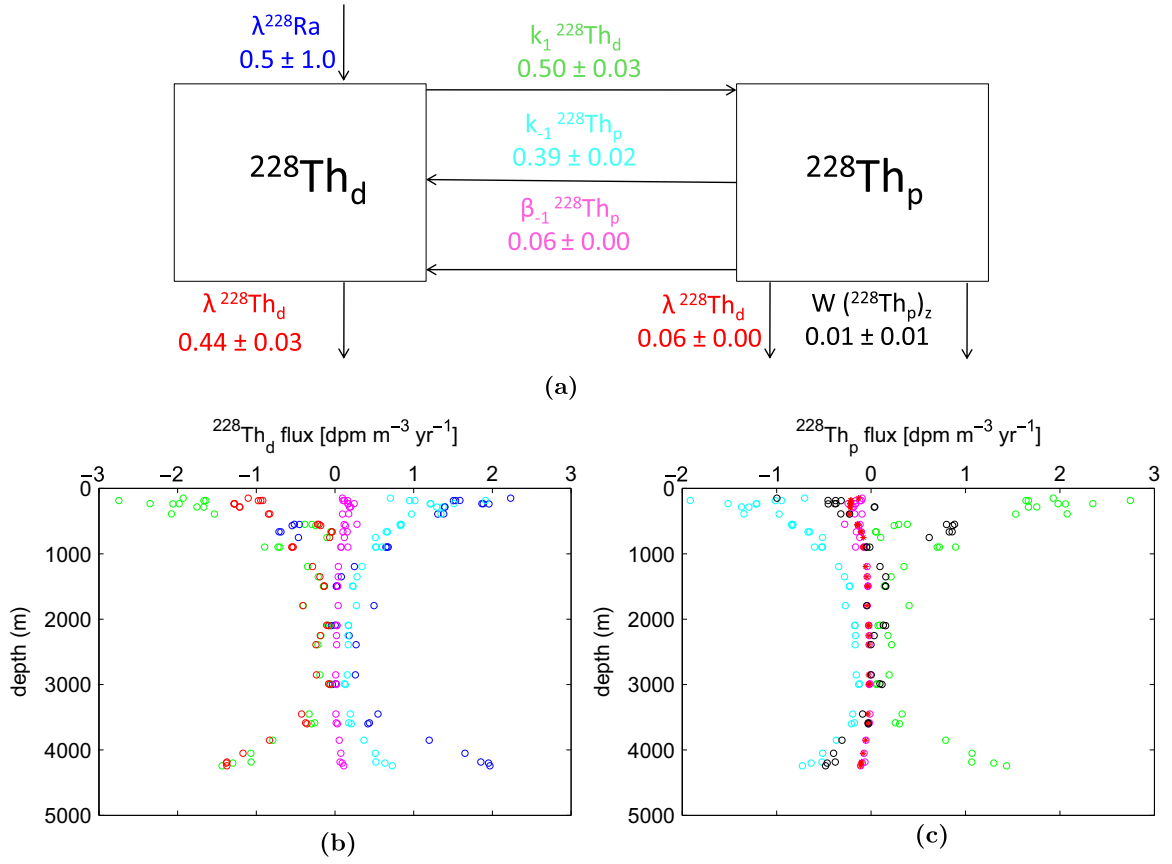
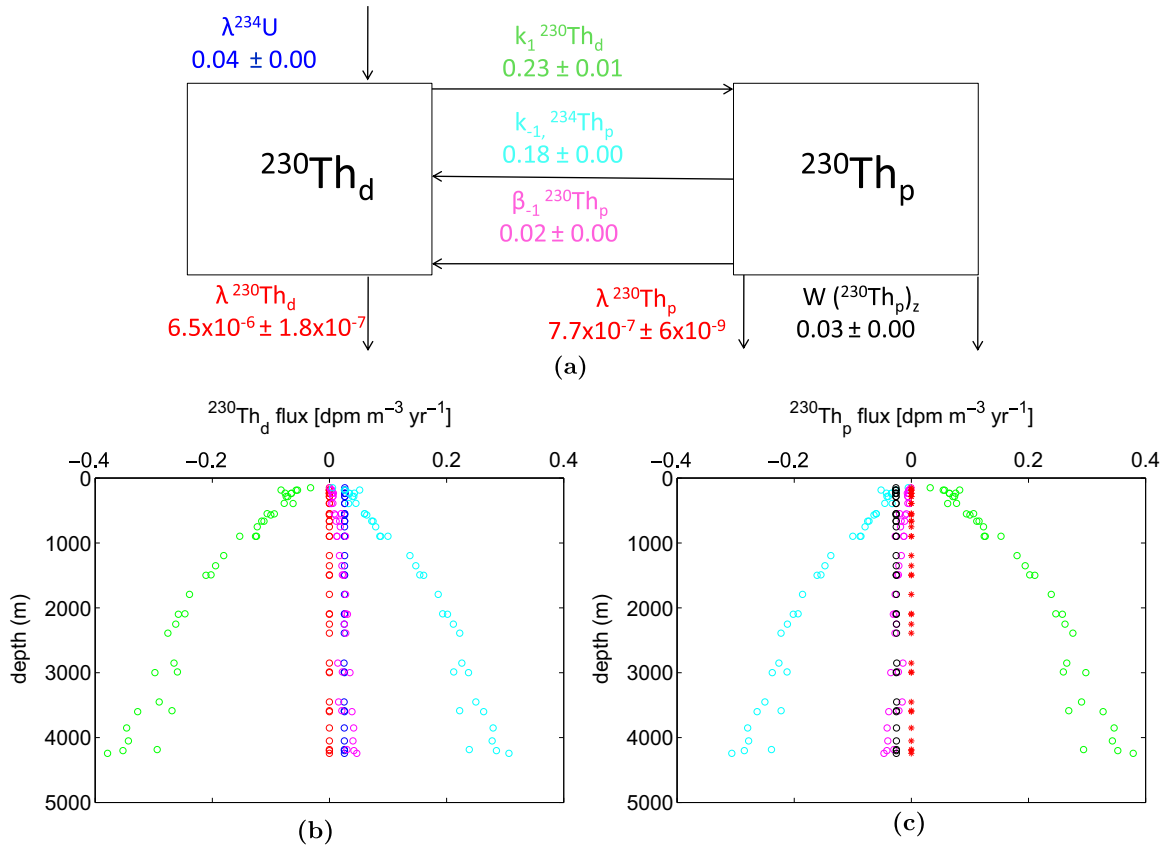**Fig. 16.** Same as Fig. 15, but for ^{228}Th.
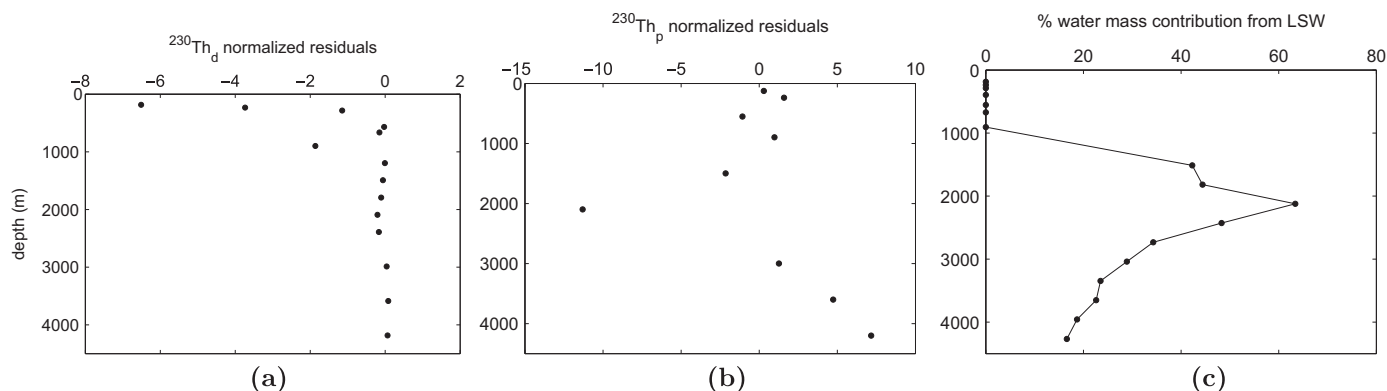

Fig. 17. Same as Fig. 15, but for ^{230}Th.

Fig. 18. Panel (a) and (b) show the normalized residuals (Eq. (11)) of $^{230}Th_d$ and $^{230}Th_p$, respectively, for our reference solution (Section 3). Panel (c) shows the sum of the proportions of Upper Labrador Sea Water and Central Labrador Sea Water at station GT11-22 (estimates from Jenkins et al., 2015).

(1993) have presented a schematic of the AABW circulation in the North Atlantic in which the bottom water flowing through the Vema Fracture Zone enters the eastern North Atlantic basins and becomes part of the NADW. Speculatively, this water may be enriched in suspended particles due to intense turbulent mixing within the fracture zone (Polzin et al., 1996; Hayes et al., 2015b).

Finally, notice that we have not shown that model V2 is a "good" model, in the sense that it is both parsimonious with parameters and does not over-fit the data. Rather our study evaluates whether the mere allowance of vertical variations in model parameters, with no change in model structure (e.g., assumption of second-order instead of first-order kinetics for Th adsorption flux) and with no additional terms in the model (e.g., horizontal transport), can significantly improve the fit to radiochemical and particle data for an open-ocean station. We show that a significantly better fit is obtained in this case (in fact, model V2 leads generally to an over-fit compared to the normal distribution) and, moreover, that some of the inferred parameters may feature systematic vertical variations suggestive of a particle concentration effect in situ.

5. Conclusion

A suite of radiochemical and particle data from station GT11-22 of the U.S. GEOTRACES North Atlantic section are used to test two versions of a particle and Th cycling model that assumes a single class of particles. Model V2, with depth-dependent rate parameters, shows a significant improvement in fit to the data set than model V1 with uniform rate parameters. In contrast to the reversible exchange model described by Bacon and Anderson (1982), we are able to

successfully tease apart desorption (k_{-1}) and remineralization (β_{-1}) by invoking a model that describes thorium as well as particle cycling in the deep ocean. We find that k_{-1} is much larger than β_{-1}, suggesting that remineralization does not result in a major loss of particulate thorium. Our analysis illustrates the pitfall of using data for a single Th isotope when testing particle and Th cycling models. It suggests the occurrence of systematic vertical variations in some of the rate constants (most notably k_1 and w) and in some of their combinations ($K = k_1/(k_{-1} + \beta_{-1})$ and $\overline{K}_{D,\beta_{-1}} = K/P$) in the mesopelagic and bathypelagic zones. It points to a significant effect of particle concentration on K and K/P in situ, i.e., k_1 and K increase with P whereas K/P decreases with P. Finally, it suggests that deviations of Th profiles from those predicted by reversible exchange, which are often interpreted in terms of an effect of ocean circulation, could be due, at least partly, to vertical variations in rate constants.

While model V2 can describe most of the GT11-22 data, it does not explain the entire data set. Features in the data that remain unexplained by model V2 include the large vertical variations of total (and hence dissolved) ^{234}Th, the kink in the particulate ^{230}Th profile near 2000 m, and the relatively uniform particle concentration below that depth. Finally, one should exercise caution when interpreting the rate parameters obtained from this study. The parameters we estimate are apparent ones that may, at least partially, mask the effects of processes not encapsulated in the model used here. We cannot rule out the presence of a bias in the inferred rate parameters, because the processes not described by the model may be the source of systematic errors. The fact that we can produce a reasonable fit to station GT11-22 data does not imply that there is no influence from other processes, such as the circulation of deep water masses, on the isotope activities and (or)
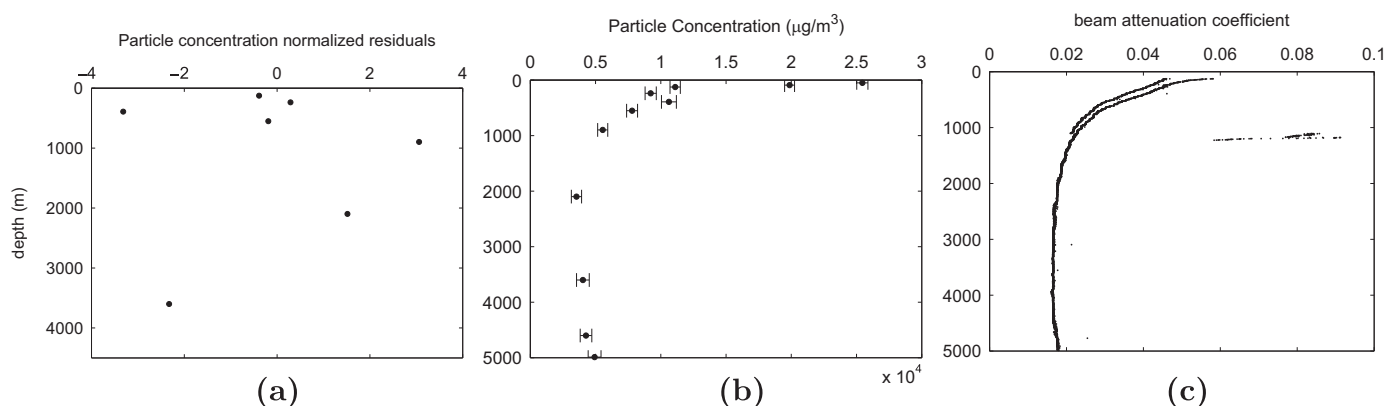

Fig. 19. Panel (a) portrays the normalized residuals for particle concentration (Eq. (11)). Panel (b) portrays the particle concentrations $\pm$ 1 standard deviation from 125 m to 4989 m, the deepest depth at which small and large particles were sampled (data from Lam et al., 2015). Panel (c) shows the beam attenuation coefficient measured using a WET Labs 25 cm pathlength C-Star transmissometer (660 nm) (data from Anderson et al., 2013). The very large values between 1000 and 1500 m are real measurements.

particle concentrations. The parameter estimates obtained in this study are only as reliable as the assumptions about data errors (C_0) and parameter distribution (S) from which these estimates have been derived

Acknowledgements

Appendix A

Table A1.

Appendix B

We use a Kolmogorov-Smirnov (KS) test (Dudewicz and Mishra, 1988) in order to test the null hypothesis that the results of our reference solution (Section 3) are not significantly different from the results derived from the changes discussed in Sections 4.1.2–4.1.5. The two-sample KS test compares the maximum vertical distance between two empirical distribution functions (DFs). This distance is used to construct the probability (p value) of rejecting a null hypothesis that is correct. The p values for each test are reported in Table B1.

With one exception, the p values all show that the two considered solutions are not significantly different. The exception is the test between our reference solution and the solution obtained

Table A1
Radiochemical and Particle Concentration Data at Station GT11-22.

Depth (m)	U	^{228}Ra	^{234}Th$_{tot}$	^{234}Th$_{p,s}$	^{234}Th$_{p,l}$	^{230}Th$_d$	^{230}Th$_{p,s}$	^{228}Th$_d$	^{228}Th$_{p,s}$	P_s	P_l	Reference
1,25,49	✓		✓									a
50		✓		✓	✓	✓		✓	✓	✓	✓	a,b,c,d
75						✓						b
84						✓						b
90		✓		✓	✓			✓	✓	✓	✓	a,c,d
124						✓						b
125	✓	✓	✓	✓	✓		✓	✓	✓	✓	✓	a,b,c,d
149	✓		✓									a
184						✓						b
185	✓		✓									a
187		✓		✓	✓			✓	✓			a,c
233						✓						b
234	✓		✓									a
237		✓		✓	✓		✓	✓	✓	✓	✓	a,b,c,d
283						✓						b
285,389	✓		✓									a
392		✓		✓	✓			✓	✓	✓	✓	a,c,d
549	✓		✓									a
551		✓		✓	✓			✓	✓	✓	✓	a,c,d
568,663						✓						b
664	✓		✓									a
751	✓		✓									a
896	✓		✓									a
897		✓		✓	✓		✓	✓	✓	✓	✓	a,b,c,d
898,1195						✓						b
1351	✓		✓									a
1492						✓						b
1498		✓		✓			✓	✓	✓			a,b,c
1793,2092						✓						b
2098		✓		✓			✓	✓	✓	✓	✓	a,b,c,d
2251,2851	✓		✓									a
2988		✓				✓		✓	✓			b,c
2998				✓			✓					a,b
3451	✓		✓									a
3568						✓						b
3600		✓		✓			✓	✓	✓	✓	✓	a,b,c,d
3851,4051	✓		✓									a
4184						✓						b
4200		✓		✓			✓	✓	✓			a,b,c
4243	✓		✓									a
4581						✓						b
4600		✓		✓			✓	✓	✓	✓	✓	a,b,c,d
4802		✓		✓			✓	✓	✓			a,b,c
4970						✓						b
4989		✓		✓			✓	✓	✓	✓	✓	a,b ,c,d

[a] ^{234}Th data from Owens et al. (2015).
[b] ^{230}Th data from Anderson et al. (2012), Hayes et al. (2015b).
[c] ^{228}Th data from Charette et al. (2015).
[d] Particle concentration data from Lam et al. (2015).

Table B1
p values from Kolmogorov-Smirnov test.

	Model-based $\hat{\boldsymbol{x}}_{k=0}$	$Th_{p,\,l}/Th_{p,s}$ = 0.07	Corrected ^{230}Th[a]	QMA bias 20%
p for V1	>0.99	>0.99	>0.99	0.98
p for V2	>0.99	0.52	>0.99	0.02

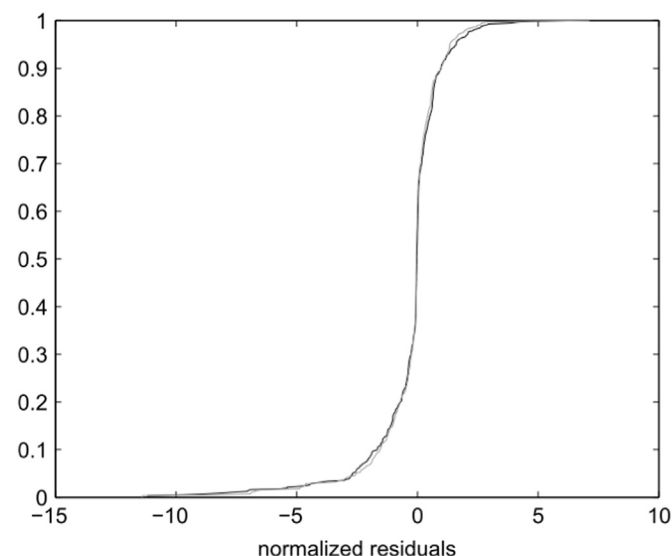[a] Measured ^{230}Th$_{d,p}$ corrected for lithogenic ^{230}Th.

Fig. B1. Normalized residuals of the fit of model V2 to station GT11-22 data for the reference case (Section 3) (black), and for the case where the prior ^{228,234}Th$_p$ values are set to 20% less than their measured values (grey).

from correcting for a potential bias in the QMA filters. Although the KS test suggests that the normalized residuals of the fit of model V2 to GT11-22 data do not have the same underlying distribution at the 5% significance level ($p=0.02$), the DFs of the two solutions look very similar (Fig. B1). Thus, in fact, the solution with reduced ^{234,228}Th$_p$ data values and the reference solution generally lead to similar results, in particular regarding the relative merits of model V1 and V2 (Table 3).

References

Alonso-González, I.J., Arístegui, J., Lee, C., Sanchez-Vidal, A., Calafat, A., Fabrés, J., Sangrá, P., Masqué, P., Hernández-Guerra, A., Benítez-Barrios, V., 2010. Role of slowly settling particles in the ocean carbon cycle. Geophys. Res. Lett. 37, 1–5.

Andersen, M.B., Stirling, C.H., Zimmermann, B., Halliday, A.N., 2010. Precise determination of the open ocean ^{234}U/^{238}U composition. Geochem. Geophys. Geosyst. 11 (12).

Anderson, R.F., Fleisher, M.Q., Robinson, L.F., Edwardds, R.L., Hoff, J., Moram, S.B., Rutgers van der Loeff, M., Thomas, A.L., Roy-Barman, M., François, R., 2012. GEOTRACES intercalibration of ^{230}Th, ^{232}Th, ^{231}Pa, and prospects for ^{10}Be. Limnol. Oceanogr. Methods 10, 179–213.

Anderson, R.F., Fleisher, M.Q., Hayes, C., 2013. Transmissometer_GTC Biological and Chemical Oceanography Data System, BCO DMO, WHOI, ⟨http://data.bco-dmo. org/jg/info/BCO/GEOTRACES/NorthAtlanticTransect/Transmissometer_GTC% 7Bdir=data.bco-dmo.org/jg/dir/BCO/GEOTRACES/NorthAtlanticTransect/,da ta=data.bco-dmo.org:80/jg/serv/BCO/GEOTRACES/NorthAtlanticTransect/ GT10-11_trans_Cp_GTC.html0%7D⟩, (accessed 22.01.15).

Armstrong, R.A., Peterson, M.L., Lee, C., Wakeham, S.G., 2009. Settling velocity spectra and the ballast ratio hypothesis. Deep Sea Res. II 56, 1470–1478.

Athias, V., Mazzega, P., Jeandel, C., 2000a. Selecting a global optimization method to estimate the oceanic particle cycling rate constants. J. Mar. Res. 58 (5), 675–707.

Athias, V., Mazzega, P., Jeandel, C., 2000b. Nonlinear inversions of a model of the oceanic dissolved-particulate exchanges, inverse methods in global biogeochemical cycles. In: Kasibhatla, P., Heimann, M., Raynar, P., Mahowald, M., Prinn, R.G., Hartley, D.E. (Eds.), Geophysical Monograph, 114. Am. Geophys. Union., United States, pp. 205–222.

Bacon, M.P., Anderson, R.F., 1982. Distribution of thorium isotopes between dissolved and particulate forms in the deep sea. J. Geophys. Res.: Oceans 87 (C3), 2045–2056 (1978 2012).

Bevington, P.R., Robinson, D.K., 1992. Data Reduction and Error Analysis for the Physical Sciences. McGraw-Hill, New York.

Bhat, S.G., Krishnaswami, S., Lal, D., Moore, W.S., 1969. ^{234}Th and ^{238}U ratios in the ocean. Earth Planet. Sci. Lett. 5, 483–491.

Bishop, J.K., 2009. Autonomous observations of the ocean biological carbon pump. Oceaonography 22 (2), 182–193.

Bishop, J.K., Lam, P.J., Wood, T.J., 2012. Getting good particles: accurate sampling of particles by large volume in situ filtration. Limnol. Oceanogr. Methods 10 (9), 681–710.

Boyle, E.A., Anderson, R.F., Cutter, G.A., Fine, R., Jenkins, W.J., Saito, M., 2015. Introduction to the US GEOTRACES North Atlantic Transect (GA-03): USGT10 and USGT11 cruises. Deep Sea Res. Part II: Top. Stud. Oceanogr. 116, 11–15.

Buesseler, K., Ball, L., Andrews, J., Cochran, J., Hirschberg, D., Bacon, M., Fleer, A., Brzezinski, M., 2001. Upper ocean export of particulate organic carbon and biogenic silica in the Southern Ocean along 170°W. Deep-Sea Res. Part II: Top. Stud. Oceanogr. 48 (19), 4275–4297.

Burd, A.B., Moran, S.B., Jackson, G.A., 2000. A coupled adsorption aggregation model of the POC/^{234}Th ratio of marine particles. Deep Sea Res. Part I: Ocean. Res. Pap. 47 (1), 103–120.

Charette, M.A., Morris, P.J., Henderson, P.B., Moore, W.S., 2015. Radium isotope Distributions during the U.S. GEOTRACES North Atlantic cruises. Mar. Chem. 177, 184–195.

Chen, J.H., Edwards, L.R., Wasserburg, G.J., 1986. ^{238}U, ^{234}U and ^{232}Th in seawater. Earth Planet. Sci. Lett. 80, 241–251.

Cheng, H., Edwards, R.L., Shen, C., Polyak, V.J., Asmerom, Y., Woodhead, J., Hellstrom, J., Wang, Y., Kong, X., Spötl, C., Wang, X., Alexandar Jr., E.C., 2013. Improvements in ^{230}Th dating, ^{230}Th and ^{234}U half-life values, and U-Th isotopic measurements by multi-collector inductively coupled plasma mass spectrometry. Earth Planet. Sci. Lett. 371, 82–91.

Clegg, S.L., Whitfield, M., 1990. A generalized model for the scavenging of trace metals in the open ocean I. Particle cycling. Deep Sea Res. Part A. Ocean. Res. A37 (5), 809–832.

Clegg, S.L., Bacon, M.P., Whitfield, M., 1991. Application of a generalized scavenging model to thorium isotope and particle data at equatorial and high-latitude sites in the Pacific Ocean. J. Geophys. Res.: Oceans 962 (C11), 20,655–20,670 (1978 2012).

Cochran, J.K., Buesseler, K.O., Bacon, M.P., Wang, H.W., Hirschberg, D.J., Ball, L., Fleer, A., 2000. Short-lived thorium isotopes (^{234}Th, ^{228}Th) as indicators of POC export and particle cycling in the Ross Sea, Southern Ocean. Deep Sea Res. Part II: Top. Stud. Oceanogr. 47 (15), 3451–3490.

Cochran, K.J., Buesseler, K.O., Bacon, M.P., Livingston, H.D., 1993. Thorium isotopes as indicators of particle dynamics in the upper ocean: results from the JGOFS North Atlantic Bloom Experiment. Deep Sea Res. Part I: Ocean. Res. Pap. 40 (8), 569–1595.

Delanghe, D., Bard, E., Hamelin, B., 2002. New TIMS constraints on the uranium-238 and uranium-234 in seawaters from the main ocean basins and the Mediterranean Sea. Mar. Chem. 80 (1), 79–93.

Dudewicz, E.J., Mishra, S.N., 1988. Modern Mathematical Statistics. John Wiley and Sons, Inc., United States.

Edmonds, H.N., Moran, S.B., Hoff, J.A., Smith, J.N., Edwards, R.L., 1998. Protactinium-231 and thorium-230 abundances and high scavenging rates in the western Arctic Ocean. Science 280 (5362), 405–407.

Efron, B., Tibshirani, R.J., 1993. An Introduction to the Bootstrap. Chapman and Hall, New York.

François, R., Frank, M., Rutgers van der Loeff, M.M., Bacon, M.P., 2004. ^{230}Th normalization: an essential tool for interpreting sedimentary fluxes during the late quaternary. Paleoceanography 19 (1).

Goldberg, E.D., 1954. Marine geochemistry 1. Chemical scavengers of the sea. J. Geol., 249–265.

Hayes, C.T., Anderson, R.F., Jaccard, S.L., François, R., Fleisher, M.Q., Soon, M., Gersonde, R., 2013. A new perspective on boundary scavenging in the North Pacific Ocean. Earth Planet. Sci. Lett. 369, 86–97.

Hayes, C.T., Anderson, R.F., Fleisher, M.Q., Vivancos, S.W., Lam, P.J., Ohnemus, D.C., Huang, K.F., Robinson, L.F., Lu, Y., Cheng, H., Edwards, R.L., Moran, B.S., 2015a. Intensity of Th and Pa scavenging partitioned by particle chemistry in the North Atlantic Ocean. Mar. Chem. 170, 49–60.

Hayes, C.T., Anderson, R.F., Fleisher, M.Q., Huang, K.F., Robinson, L.F., Lu, Y., Cheng, H., Edwards, L.R., Moran, B.S., 2015b. ^{230}Th and ^{231}Pa on GEOTRACES GA03, the U.S. GEOTRACES North Atlantic transect, and implications for modern and paleoceanographic chemical fluxes. Deep Sea Res. Part II: Top. Stud. Oceanogr. 116, 29–41.

Henderson, P.B., Morris, P.J., Moore, W.S., Charette, M.A., 2013. Methodological advances for measuring low-level radium isotopes in seawater. J. Radio. Nucl. Chem. 296 (1), 357–362.

Honeyman, B.D., Santschi, P.H., 1989. A Brownian-pumping model for oceanic trace metal scavenging: evidence from Th isotopes. J. Mar. Res. 47 (4), 951–992.

Honeyman, B.D., Balistrieri, L.S., Murray, J.W., 1988. Oceanic trace metal scavenging: the importance of particle concentration. Deep Sea Res. Part A. Ocean. Res. Pap. 35 (2), 227–246.

Jenkins, W.J., Smethie, W.M., Boyle, E.A., 2015. Water mass analysis for the U.S. GEOTRACES North Atlantic Sections. Deep Sea Res. Part II: Top. Stud. Oceanogr. 116, 6–20.

Kendall, M., Gibbons, J.D.R., 1990. Rank Correlation Methods. Oxford University Press, Oxford.

Kirby, H.W., Grove, G.R., Timma, D.L., 2002. Neutron-capture cross section of actinium-227. Phys. Rev. 102 (4), 1140–1141.

Knight, G.B., Macklin, R.L., 1948. Half-Life of UX1 (Th-234). Phys. Rev. 74 (10), 1540–1541.

Krauskopf, K.B., 1956. Factors controlling the concentrations of thirteen rare metals in sea-water. Geochim. Cosmochim. Acta 9 (1) 1–B32.

Krishnaswami, S., Lal, D., Somayajulu, B.L.K., Weiss, R.F., Craig, H., 1976. Large-volume in-situ filtration of deep Pacific waters: mineralogical and radioisotope studies. Earth Planet. Sci. Lett. 32 (2) 1–B32.

Krishnaswami, S., Sarin, M.M., Somayajulu, B.L.K., 1981. Chemical and radiochemical investigations of surface and deep particles of the Indian Ocean. Earth Planet. Sci. Lett. 51 (1), 81–96.

Ku, T.L., Knauss, K.G., Mathieu, G.G., 1977. Uranium in open ocean: concentration and isotopic composition. Deep Sea Res. 24 (12), 31–39.

Kumar, N., Gwiazda, R., Anderson, R., Froelich, P., 1993. $^{231}Pa/^{230}Th$ ratios in sediments as a proxy for past changes in Southern Ocean productivity. Nature 362 (6415), 45–48.

Kumar, N., Anderson, R., Mortlock, R., Froelich, P., Kubik, P., Dittrich-Hannen, B., Suter, M., 1995. Increased biological productivity and export production in the glacial Southern Ocean. Nature 378 (6558), 675–680.

Lam, P., Marchal, O., 2014. Insights into particle dynamics from the geochemical composition of suspended and sinking particles. Annu. Rev. Mar. Sci. 7 (1), 12.1–12.26.

Lam, P.J., Ohnemus, D.C., Auro, M.E., 2015. Size-fractionated major particle composition and concentration from the U.S. GEOTRACES North Atlantic zonal transect. Deep-Sea Res. II 116, 303–320.

Lee, C., Peterson, M.A., Wakeham, S.G., Armstrong, R.A., Cochran, J.K., Miquel, J.C., Fowler, S.W., Hirschberg, D., Beck, A., Xue, J., 2009. Particulate organic matter and ballast fluxes measured using time-series and settling velocity sediment traps in the northwestern Mediterranean Sea. Deep Sea Res. II 56, 1420–1436.

Maiti, K., Buesseler, K.O., Pike, S.M., Benitez-Nelson, C., Cai, P., Chen, W., Cochran, K., Dai, M., Dehairs, F., Gasser, B., Kelley, R.P., Masque, P., Miller, L.A., Miquel, J.C., Moran, S.B., Morris, P.J., Peine, F., Planchon, F., Renfo, A.A., Rutgers van der Loeff, M., Santschi, P.H., Turnewitsch, R., Waples, J.T., Xu, C., 2012. Intercalibration studies of short-lived thorium-234 in the water column and marine particles. Limnol. Oceanogr. Methods 10 (9), 631–644.

Maiti, K., Charette, M.A., Buesseler, K.O., Zhou, K., Henderson, P., Moore, W.S., Morris, P., Kipp, L., 2015. Determination of particulate and dissolved ^{228}Th in seawater using a delayed coincidence counter. Mar. Chem. 177, 196–202.

Marchal, O., Lam, P.J., 2012. What can paired measurements of Th isotope activity and particle concentration tell us about particle cycling in the ocean? Geochim. Cosmochim. Acta 90, 126–148.

Marchal, O., François, R., Scholten, J., 2007. Contribution of ^{230}Th measurements to the estimation of the abyssal circulation. Deep Sea Res. Part I: Ocean. Res. 54 (4), 557–585.

Mawji, E., et al., 2015. The GEOTRACES intermediate data product 2014. Mar. Chem. 177 (Part 1), 1–8.

McCartney, M.S., Bennett, S.L., Woodgate-Jones, M.E., 1991. Eastward flow through the Mid-Atlantic Ridge at 11°N and its influence on the abyss of the eastern basin. J. Phys. Ocean. 21 (8), 1089–1121.

McDonnell, A.M., Buesseler, K.O., 2010. Variability in the average sinking velocity of marine particles. Limnol. Oceanogr. 55 (5), 2085–2096.

Mercier, H., 1986. Determining the general circulation of the ocean: a nonlinear inverse problem. J. Geophys. Res.: Oceans 91 (C4), 5103–5109 (1978–2012).

Mercier, H., 1989. A study of the time-averaged circulation in the western North Atlantic by simultaneous nonlinear inversion of hydrographic and current meter data. Deep Sea Res. Part A. Ocean. Res. Pap. 36 (2), 297–313.

Mercier, H., Ollitrault, M., Le Traon, P.Y., 1993. A study of the time-averaged circulation in the western North Atlantic by simultaneous nonlinear inversion of hydrographic and current meter data. J. Phys. Oceanogr. 23 (4), 689–715.

Moran, S.B., Charette, M.A., Hoff, J.A., Edwards, R.L., Landing, W.M., 1997. Distribution of ^{230}Th in the Labrador Sea and its relation to ventilation. Earth Planet. Sci. Lett. 150 (1), 151–160.

Moran, S.B., Shen, C.C., Edmonds, H.N., Weinstein, S.E., Smith, J.N., Edwards, R.L., 2002. Dissolved and particulate ^{231}Pa and ^{230}Th in the Atlantic Ocean: constraints on intermediate/deep water age, boundary scavenging, and $^{231}Pa/^{230}Th$ fractionation. Earth Planet. Sci. Lett. 203 (3), 999–1014.

Murnane, R.J., 1994. Determination of thorium and particulate matter cycling parameters at station P: a reanalysis and comparison of least squares techniques. J. Geophys. Res.: Oceans 99 (C2), 3393–3405.

Murnane, R.J., Sarmiento, J.L., Bacon, M.P., 1990. Thorium isotopes, particle cycling models, and inverse calculations of model rate constants. J. Geophys. Res.: Oceans 95 (C9), 16195–16206.

Murnane, R.J., Cochran, J.K., Sarmiento, J.L., 1994. Estimates of particle-and thorium-cycling rates in the northwest Atlantic Ocean. J. Geophys. Res.: Oceans 99 (C2), 3373–3392.

Murnane, R.J., Cochran, J.K., Buesseler, K.O., Bacon, M.P., 1996. Least-squares estimates of thorium, particle, and nutrient cycling rate constants from the JGOFS North Atlantic Bloom Experiment. Deep Sea Res. Part I: Ocean. Res. Pap. 43 (2), 239–258.

Nozaki, Y., Nakanishi, T., 1985. ^{231}Pa and ^{230}Th profiles in the open ocean water column. Deep Sea Res. Part A. Ocean. Res. Pap. 32 (10), 1209–1220.

Nozaki, Y., Horibe, Y., Tsubota, H., 1981. The water column distributions of thorium isotopes in the western North Pacific. Earth Planet. Sci. Lett. 54 (2), 203–216.

Nozaki, Y., Yang, H.-S., Yamada, M., 1987. Scavenging of thorium in the ocean. J. Geophys. Res.: Oceans 92 (C1), 772–778 (1978 2012).

Ohnemus, D.C., Lam, P.J., 2015. Cycling of lithogenic marine particulates in the US GEOTRACES North Atlantic Zonal transect. Deep Sea Res. II 116, 283–302.

Okubo, A., Obata, H., Gamo, T., Yamada, M., 2012. ^{230}Th and ^{232}Th distributions in mid-latitudes of the North Pacific Ocean: effect of bottom scavenging. Earth Planet. Sci. Lett. 339, 139–150.

Owens, S.A., Buesseler, K.O., Sims, K.W.W., 2011. Re-evaluating the ^{238}U-salinity relationship in seawater: implications for the ^{238}U ^{234}Th disequilibrium method. Mar. Chem. 126 (1), 31–39.

Owens, S.A., Buesseler, K.O., Pike, S., 2015. Thorium-234 as a tracer of particle dynamics and upper ocean export in the Atlantic Ocean. Deep Sea Res.-II 116, 42–59.

Paillet, J., Mercier, H., 1997. An inverse model of the eastern North Atlantic general circulation and thermocline ventilation. Deep Sea Res. Part I: Ocean. Res. Pap. 44 (8), 1293–1328.

Polzin, K., Speer, K., Toole, J., Schmitt, R., 1996. Intense mixing of Antarctic bottom water in the equatorial Atlantic Ocean. Nature 380, 54–57.

Roy-Barman, M., Coppola, L., Souhaut, M., 2002. Thorium isotopes in the western Mediterranean Sea: an insight into the marine particle dynamics. Earth Planet. Sci. Lett. 196 (3), 161–174.

Rutgers van der Loeff, M., Berger, G.W., 1993. Scavenging of ^{230}Th and ^{231}Pa near the Antarctic polar front in the South Atlantic. Deep Sea Res. Part I: Ocean. Res. Pap. 40 (2), 339–357.

Savoye, N., Benitez-Nelson, C., Burd, A.B., Cochran, J.K., Charette, M., Buesseler, K.O., Jackson, G.A., Roy-Barman, M., Schmidt, S., Elsken, M., 2006. ^{234}Th sorption and export models in the water column: a review. Mar. Chem. 100, 234–249.

Schmitz, W.J., McCartney, M.S., 1993. On the North Atlantic circulation. Rev. Geophys. 31 (1), 29–49.

Scholten, J.C., Rutgers, M., Van Der Loeff, M.A., 1995. Distribution of ^{230}Th and ^{231}Pa in the water column in relation to the ventilation of the deep Arctic basins. Deep Sea Res. Part II: Top. Stud. Oceanogr. 42 (6), 1519–1531.

Scholten, J.C., Fietzke, J., Mangini, A., Garbe-Schönberg, C.-D., Eisenhauer, A., Schneider, P., Stoffers, P., 2008. Advection and scavenging: effects on ^{230}Th and ^{231}Pa distribution off Southwest Africa. Earth Planet. Sci. Lett. 271, 159–169.

Shen, C.C., Wu, C.C., Cheng, H., Edwards, R.L., Hsieh, Y.T., Gallet, S., Chang, C.C., Li, T. Y., Lam, D.D., Kano, A., Hori, M., Spotl, C., 2012. High-precision and high-resolution carbonate ^{230}Th dating by MC-ICP-MS with SEM protocols. Geochim. et. Cosmochim. Acta 99, 71–86.

Stramma, L., Sabine, H., Schafstall, J., 2005. Water masses and currents in the upper tropical Northeast Atlantic off Northwest Africa. J. Geophys. Res: Oceans 110 (C12), 1–18.

Tarantola, A., Valette, B., 1982. Generalized nonlinear inverse problems solved using the least squares criterion. Rev. Geophys. 20 (2), 219–232.

Turekian, K.K., 1977. The fate of metals in the ocean. Geochim. Cosmochim. Acta 41 (8), 1139–1144.

Turner, J.T., 2002. Zooplankton fecal pellets, marine snow and sinking phytoplankton blooms. Aquat. Microb. Ecol. 27 (1), 57–102.

Vanmarcke, E., 1983. Random Fields: Analysis and Synthesis. MIT Press, Cambridge.

Venchiarutti, C., Jeandel, C., Roy-Barman, M., 2008. Particle dynamics study in the wake of Kerguelen Island using thorium isotopes. Deep Sea Res. Part I: Ocean. Res. Pap. 55 (10), 1343–1363.

Vogler, S., Scholten, J., Rutger van der Loeff, M., Mangini, A., 1998. ^{230}Th in the eastern North Atlantic: the importance of water mass ventilation in the balance of ^{230}Th. Earth Planet. Sci. Lett. 156 (1), 61–74.

Wolberg, J.R., 1967. Prediction Analysis. D. Van Nostrand, Princeton.

Wunsch, C., 2006. Discrete Inverse and State Estimation Problems: with Geophysical Fluid Applications, 2. Cambridge University Press, Cambridge.

Yu, E.-F., François, R., Bacon, M.P., 1996. Similar rates of modern and last-glacial ocean thermohaline circulation inferred from radiochemical data. Nature 379, 689–694.